Colloids and Surfaces A: Physicochemical and Engineering Aspects 624 (2021) 126760

Contents lists available at ScienceDirect

Colloids and Surfaces A: Physicochemical and Engineering Aspects

journal homepage: www.elsevier.com/locate/colsurfa

Application of Pickering emulsions in 3D printing of personalized nutrition. Part II: Functional properties of reduced-fat 3D printed cheese analogues

Mahdiyar Shahbazi [a,*], Henry Jäger [a,*], Rammile Ettelaie [b]

[a] Institute of Food Technology, University of Natural Resources and Life Sciences (BOKU), Muthgasse 18, 1190 Vienna, Austria
[b] Food Colloids and Bioprocessing Group, School of Food Science and Nutrition, University of Leeds, Leeds LS2 9JT, UK

HIGHLIGHTS

- A highly porous 3D structure was fabricated in presence of micro-biosurfactant.
- Reduced-fat 3D printed objects formed a structured and stable network.
- Reduced-fat 3D printed objects presented greater stability against freezing.
- The presence of micro-biosurfactant offered a better lubrication effect in 3D printed constructs.
- Reduced-fat 3D printed samples showed a desired sensory profile with a higher creamy sensation.

GRAPHICAL ABSTRACT

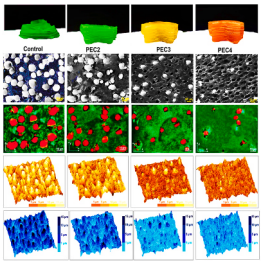

ARTICLE INFO

Keywords:
3D printing
Freeze-thaw stability
XRD
NMR
Oral tribology
Dynamic sensory evaluation

ABSTRACT

The current interest in personalized food through the application of surface-active biopolymers and additive manufacturing has identified a requirement to tailor a 3D printed healthy diet with well-defined geometries. In this study, a reduced-fat casein-based Pickering emulsion was stabilized via different ratios of acetylated microcrystalline cellulose, and then it was printed through an extrusion-based printer. The micro-biosurfactant contents led to differences in the printing performance and resolution of printed architectures. The original compact and uneven structures of 3D printed objects were reduced in presence of micro-biosurfactant, providing a uniform and porous matrix. Thermal investigation indicated that oil and aqueous phases in the reduced-fat 3D printed systems were less readily frozen. Proton molecular mobility became less mobile and moved to the populations with a shorter relaxation time upon micro-biosurfactant addition. Oral tribology was shown to depend on micro-biosurfactant content, where less deformable (firmer) 3D printed objects decreased surface-surface contact and reduced friction coefficients, improving lubrication property. The dynamic sensory evaluation by temporal dominance of sensations showed promising results regarding creaminess and mouth-coating, which was correlated well with instrumental readings. This work established an integrated attitude, from fundamental and practical viewpoints, supporting the application of Pickering emulsions in the 3D printing process to develop functional foods, broadening the micro-biosurfactant utilization in food printing.

* Correspondence to: Institute of Food Technology, Department of Food Science and Technology, University of Natural Resources and Life Sciences, Muthgasse 18, 1190 Vienna, Austria.
E-mail addresses: shahbazim00@yahoo.com, m.shahbazi1366@gmail.com (M. Shahbazi), henry.jaeger@boku.ac.at (H. Jäger).

https://doi.org/10.1016/j.colsurfa.2021.126760
Received 7 March 2021; Received in revised form 21 April 2021; Accepted 28 April 2021
Available online 4 May 2021

1. Introduction

Three-dimensional (3D) printing or rapid prototyping is an innovative technique leading to the fabrication of intricate geometries from 3D model data, commonly layer-by-layer. The process launches using a 3D design (meshed) model that can be developed with attained image data or structures created in computer-aided design (CAD) software. In this regard, an STL (Surface Tessellation Language) file format for the design of virtual objects is usually produced. The meshed data can be sliced into model layers with special software and sent to the printing system [1,2]. An important aspect of engineering constructs through 3D printing rather than traditional manufacturing approaches is waste reduction, supporting end-users needs aligned with sustainability-oriented issues [3]. Thanks to the inherently limited structural strength and functionalities of printed constructs manufactured from biomaterials, there is an essential need to develop a reinforced printable ink to develop a well-defined 3D structure with improved printability. In this scenario, an effective route to manufacturing a stable and custom-tailored printed object is the extrusion of inks in form of colloidal dispersions. Recently, this method has attracted substantial attention on account of offering the selection of an extensive variety of biomaterials and operating under ambient processing conditions [4–6].

In recent years, the development of Pickering emulsions using sustainable cellulose derivatives, including microcrystalline cellulose (MCC) has also gained considerable attention because of their low toxicity, renewability, and biodegradability [7,8]. Nevertheless, unmodified MCC suffers from poor adsorption ability at the O/W interface and aggregation of its hydrophilic groups, which makes it difficult to apply as an efficient stabilizer [9,10]. It was shown that MCC can be surface-modified by hydrophobic groups to enhance its colloidal stability and reducing aggregation, thus reinforcing the emulsification properties [11–13]. Therefore, the hydrophobically modified MCC can be utilized for the preparation of an effective Pickering emulsion with the desired compatibility and enhanced interfacial adhesion between the hydrophilic and hydrophobic phases.

Over the years, the image of processed cheese analogues alters from an inferior quality product to a personalized product, fulfilling consumers' expectations concerning a healthy diet and nutritious food. In recent years, the applications of casein to produce processed cheeses have widened from the traditional process to more cutting-edge technology such as 3D printing [14,15]. A large number of research studies on 3D printed cheese products highlights the recent increased attention to develop novel functionalities to satisfy specific end-use application [15–17]. Daffner et al. [16] printed a casein/whey protein multisystem ink by using an extrusion-based 3D printer for tailored nutrition application. Liu et al. [18] produced a 3D printed construct by printing a blended ink based on milk protein concentrate/casein with desirable printability. In another work, a 3D printed casein structure was manufactured through fused deposition modeling technique with well-defined 3D printed constructs [17].

There is an increasing consumer pressure to produce commercial foods that are more organic, sustainable, and personal care products. In this regard, the preparation of personalized foods includes sound analysis of individual requirements, assembling a distinct nutrition profile, and optional post-processing operations [2]. Application of the reduced-fat Pickering emulsions in the 3D food printing can pave the way towards tailor-made personalized nutrition according to an individual health condition. It is essentially promising as providing wholesome products for population groups with specific needs (athletes, vegetarian community, elderly, pregnant, etc.). Although several studies have investigated the utilization of 3D printing in engineering food products, there is no study focused on the possibility of using Pickering emulsions to manufacture the 3D printed products with individual preferences.

According to our findings described in Part I of the preceding study [10], the optimum physical, rheological, and structural features to achieve the superior formulation aimed at producing a reduced-fat printable ink were determined. In this sense, Pickering emulsions containing higher levels of acetylated MCC were shown an ideal ink in terms of shear-thinning, viscoelastic, thixotropic, and thermoreversible properties. It was then concluded the *pseudoplastic* inks characterized by solid-like structure and recoverable network might be easily extruded from a nozzle tip and providing enough mechanical strength to resist deformation after deposition.

The hypothesis of this study was based on the fact that reduced-fat casein-based emulsion stabilized by acetylated MCC can be effectively printed in a 3D fashion with stable structural properties. Accordingly, oil was partially substituted by acetylated MCC in the casein-based emulsion, and then the produced inks were printed via an extrusion-based printer. Afterward, the changes in the functional properties of 3D printed constructs were studied in terms of printing performance, microstructure, textural properties, freeze-thaw stability, crystalline pattern, oral tribology features, and temporal dominance of sensation (TDS) method. Since instrumental measurements need to be validated with sensory assessment, a correlation among instrumental variables and TDS scores obtained by dynamic sensory evaluation was also performed.

2. Methods and materials

2.1. Materials

Materials were presented and characterized comprehensively in the previous publication [10]. Briefly, sodium caseinate was supplied by Fonterra Research and Development Centre (Palmerston North, New Zealand). The MCC Avicel® PH-101, calcium chloride, analytical grade sodium hydroxide, hydrochloric acid, ethanol, imidazole, and sodium azide were purchased from Sigma (Sigma-Aldrich GmbH, Sternheim, Germany). Canola oil, olive oil, and sodium chloride were provided from a local market and used without further purification. Cheese flavor agent was obtained from Edlong® (Cork, Ireland).

2.2. Preparation of Pickering emulsion inks

The casein-based ink was developed using the replacement of canola oil by acetylated MCC as described in Part I of this series [10]. Briefly, a buffer solution was prepared using dispersing 4 mM acetic acid and imidazole into the water and then adjusting the pH to 7.0 by 1 M NaOH. Initially, sodium caseinate hydration was completed through dispersing powdered sodium caseinate (18 wt%) into 5 mM imidazole/acetate buffer (pH 7.0) and heated to 90 °C and held at this temperature for 1 min. Then, the dispersion was stirred at 35 °C overnight to ensure complete hydration. Simultaneously, stock suspension of acetylated MCC (named as AMCC) was obtained by dispersing weighed amount (70 wt% AMCC) of the AMCC into the same buffer (pH 7.0) and homogenized with a high-speed rotor-stator device (Ultra-Turrax T25D IKA, Germany) at a shear rate of 56/s (367 G-force). After that, the AMCC suspension was stirred overnight at ambient conditions. The pH of this suspension was then adjusted back to pH 7.0.

An O/W emulsion was then obtained by blending canola oil (10 wt%) and (90 wt%) aqueous sodium caseinate (18 wt% sodium caseinate, pH 7.0) using a high-speed blender (Ultra-Turrax T25D IKA, Germany). At the same time, NaCl (0.3 wt%) was introduced into the system. Next, the coarse emulsion was passed through a two-stage high-pressure Microfluidizer processor (M110-PS, Microfluidics international Corp., Newton, MA) with 180 bar at the first phase and 76 bar at the second phase. The full-fat homogenized ink referred to as control hereinafter (10 wt% canola oil, 18 wt% sodium caseinate, pH 7.0) was employed to develop reduced-fat inks. On this subject, 15%, 30%, 45%, and 60% reduced-fat inks were made with AMCC stock suspension (70 wt% AMCC, pH 7.0) to develop Pickering emulsions with the following compositions: 8.5 wt% canola oil and 1.05 wt% AMCC (PEC1), 7 wt% canola oil and 2.1 wt% AMCC (PEC2), 5.5 wt% canola oil and 3.15 wt%

AMCC (PEC3), and 4 wt% canola oil and 4.2 wt% AMCC (PEC4). The casein ratio was considered constant in all formulations (18 wt%). Furthermore, the amount of 0.1 wt% cheese flavor agent was added to all formulations. Finally, 0.005 wt% sodium azide was added to the casein-based inks as an antimicrobial agent. The obtained Pickering inks were poured into plastic containers and stored overnight at 4 °C [10].

2.3. Printing process

An extrusion-based system (Mycusini®, Procusini, Freising, Germany) was used to print casein-based inks in a layer-by-layer fashion. Different geometrical designs (heart, cylindrical, and star) were modeled and converted to an STL file through a computer-aided design software (AutoCAD; Autodesk Inc., San Rafael, CA). The different architectural designs of 3D printed samples allowed to better evaluation of printing performance and 3D structure quality properties between the printed object variants. To provide the XYZ pathway instructions of the 3D printer, the G-code files were created using the open-source CAM software Slic3r (slic3r.org, consulted on December 2020) from the STL file. The casein-based inks (10 mL) were poured into a stainless-steel cartridge. The filled cartridge was then vigorously stirred by a Vortex mixer (Thermo Fisher Scientific, San Jose, CA) for 15 min to remove the air bubbles from the emulsions [19]. The printing settings were set according to the preliminary investigations to assess the effect of different contents of micro-biosurfactant on the printing performance. The number of deposited layers was 20, layer height was set at 1 mm, and the width of the tip was considered 1 mm. The height of the tip was increased by 1.1 mm after the deposition of each layer. After printing, each 3D printed architecture was covered with an aluminum cover plate and stored at 4 °C to avoid dehydration. Table 1 summarizes the printing settings used to examine the printing performance of the casein-based inks.

2.4. Characterization of 3D printed cheese analogues

2.4.1. Printing performance

The printing performance of 3D printed objects upon replacement of oil by different ratios of micro-biosurfactant was performed. The 3D printed constructs were transferred to a specific chamber (20 cm × 20 cm × 20 cm), which was equipped with a camera (Alpha 7M3 E-Mount, Full-Frame Mirrorless, 24.2 MP, Sony, Tokyo, Japan) to take photos. Five replicates of each printed object were considered to determine the line width and layer number through a digital caliper (Mitutoyo, Absolute Digimatic, Tokyo, Japan) [1].

2.4.2. Morphological investigations

To obtain detailed high-resolution morphology with a high-depth of field, the microstructure of 3D printed architectures was assessed through a variable-pressure scanning electron microscope (VP-SEM Quanta 200 FEG SEM, FEI Company, Eindhoven, Netherlands). The 3D printed objects were cut to a proper size (20 mm × 20 mm × 20 mm). Afterward, the samples were mounted on a Peltier-cooled holder at − 18 °C to avoid thermal damage. The nitrous oxide was used as imaging gas, providing a pressure of ~50.7 Pa. The morphology of 3D printed structures was captured with a solid-state backscatter detector using the accelerating voltage of 20 kV [20].

Confocal laser scanning microscopy (CLSM) observation was performed through an FV-300 confocal scanning instrument (Olympus, Tokyo, Japan) equipped with an Olympus IX71 inverted microscope and an argon-ion laser. Before evaluation, the 3D printed samples were stained with a 0.5 wt% blended fluorescent colorant solution (Nile Red and Nile Blue). Next, the stained 3D printed objects were transferred to the slide and enclosed by a cover slide. The CLSM image of each 3D printed construct was measured by selectively exciting at 488 nm for Nile Red and 633 nm for Nile Blue.

A digital atomic force microscope (AFM, VEECO Dimension 3100, NY, USA) with Budget Sensors Tap300Al-G cantilevers was employed to study the topographic properties of 3D printed objects. The resonance frequency of 350 kHz was applied in the tapping mode with a spring constant of 45 N m^{-1} resonance. To analyze the height and phase differences in 3D printed objects, the AFM probe of the etched silicon tip was employed. Each printed variant was fixed onto a softly heated glass slide. The AFM investigation was carried out at a temperature of 22 °C and relative humidity of (34.6 ± 0.5%). The scan size of (50 × 50) μm^2 was applied for all roughness assessments, which provided appropriate sampling and offered a direct comparison of main surface properties. In this regard, the roughness variables including average roughness (R_a) and root-mean square roughness (R_q) were determined [21,22].

2.4.3. Textural properties

The textural parameters of 3D printed cheese analogues were taken into account including hardness, cohesiveness, gumminess, springiness, and chewiness obtaining from a force-deformation plot through a texture analyzer (TA.XT-plus, Stable Micro Systems, Godalming, UK). The 3D printed samples were sectioned as cylindrical shape (30 × 30) mm^2 and then compressed with a cylindrical probe (75 mm diameter) based on the TPA method. The device was set at 5 mm s^{-1} with a distance of 8 cm and a peak force of 15 N. The maximum force employed was considered as hardness. The cohesiveness was determined by the proportion of positive force zone upon the second compression step during the first compression phase. The gumminess was determined from multiplying hardness in the cohesiveness amount. The springiness was considered as the height recovered upon the period between the completion of the initial compression and the beginning of the second compression. The chewiness was finally measured as gumminess × springiness. All TPA variables were assessed via the Exponent Lite software (v.6.1.4, TA.XT-plus, Stable Micro Systems, Godalming, UK) [22].

2.4.4. Differential scanning calorimetry (DSC)

The thermal behavior of the 3D printed objects as affected by biosurfactant ratios was assessed through a differential scanning calorimeter (DSC-Q100, TA Instruments, New Castle, DE). A tiny amount (approximately 5 mg) of 3D printed samples were located on an aluminum pan, and then the measurements were conducted first by heating from − 40 to 120 °C, followed by cooling from 120 °C to − 60 °C. All evaluations were performed with a heating rate of 10 °C min^{-1} under oxygen-free nitrogen with a flow rate of 40 mL min^{-1}. The thermal variables including melting peak (*Tm*), peak enthalpy, and crystallization peak (*Tc*) were automatically measured by TA Data Analysis software (TA Instruments, New Castle, DE) [22].

2.4.5. X-ray diffraction pattern

The crystalline pattern and relative crystallinity of the 3D printed

Table 1
A summary of printing settings expressed as Slic3r terms (http://slic3r.com).

Printing adjusting	Sign	Value	Units	Definition
Nozzle diameter	D	1.0	mm	Nozzle diameter
Layer height	Z	1.0	mm	Layer height
Extrusion flow speed	Q	0.40	mL min^{-1}	Continuous extrusion flow rate provided by the syringe pump
Flow rate	S	90	%	The volume of ink that passes through the extruder
Infill velocity	V	15	mm s^{-1}	Spindle speed during extrusion
Travel velocity	V_{travel}	180	mm s^{-1}	The spindle speed of a jump between the end of one extrusion and the next
Perimeter	P	10	–	Number of outline layers
Infill density	ρ_{infill}	90	%	Quantity of material filling the object

cheese analogues were investigated by an X-ray diffraction instrument (XRD, Philips X-Pert PRO, Netherlands). The assessment was carried out with 40 kV energy, 30 mA current, and Cu Kα irradiation ($\lambda = 1.54056$ Å). Each 3D printed object was irradiated from 2° to 55° and scanned with a speed of 0.018° min^{-1} at ambient conditions [19,23]. To examine the relative crystallinity degree (RCD), total curve area (I_t) and the area under the peaks (I_p) were obtained using the software provided by X′pert Highscore Plus (v2.0, PANalytical, The Netherlands), and RCD was then calculated from Eq. (1):

$$RCD(\%) = (I_p/I_t) \times 100 \quad (1)$$

2.4.6. Time-domain nuclear magnetic resonance (TD NMR)

The free induction decay (FID) and Carr-Purcell-Meiboom-Gill (CPMG) were detected through a low resolution (20 MHz) ^{1}H TD NMR spectrometer (MiniSpec MQ 20 TD, Bruker, Rheinstetten, Germany). The TD NMR instrument was coupled with a circulating water bath to keep the cell temperature at 20 °C. The 3D printed objects (about 0.5 g) were moved to an NMR tube. Transverse relaxation curves were determined through an FID single pulse (T_2 between 1 and 1000 μs) and a CPMG pulse sequence (T_2 between 1 and 1000 ms). Regarding FID, the pulse width of the single 90° pulse was 2.86 μs, in which 1000 data points were obtained. Concerning CPMG, the pulse lengths were detected in 2.68 μs for the 90° pulse and 5.24 μs for the 180° pulse, separating by an interpulse spacing of 0.1 ms, through which 2500 data points were collected. Each relaxation curve was fitted to a continuous distribution of exponentials by the CONTIN algorithm of Provencher with the Bruker software (Bruker, Rheinstetten, Germany) [24,25].

2.4.7. Oral tribology measurements

Saliva has an important effect on oral lubrication and must be introduced in a tribological experiment aimed at a desired simulate of the in vivo circumstances. The unstimulated whole saliva (4 mL) was collected according to established work by Navazesh [26] with some modification. In short, ten non-smoker participants (five females and five males) were trained to refrain from eating or drinking (excluding water) for 2 h before the saliva collection in the morning (10 a.m.). Next, the participants were requested to rinse their mouth with water four times, and then saliva was collected by chewing a silicone cube (35 mm diameter). The participants put the cube in their mouth with water (5 mL) and started to chew for 40 s and then expectorated. In the end, they were asked to continue chewing for 50 s, simultaneously collecting saliva in a 100 mL sterile container served in ice. Approximately 4 mM imidazole/acetate buffer (pH 7.0) was added to the freshly collected saliva (1:1 v/v) and centrifuged (Beckman, GS-15R Palo Alto, CA) at 2000 G-force for 5 min. The imidazole/acetate buffer (pH 7.0) was further incorporated into the supernatant to dilute it to 16 (v/v)% of the unstimulated whole human saliva for the tribological analyses and stored at − 18 °C for further test.

To evaluate the lubricant properties of the 3D printed objects, oral tribology evolution of saliva (*ex vivo*) was performed using a ring-on-plate tribo-rheometry (TA Instrument, New Castle, DE) on a rough hydrophobic surface of 3M Transpore Surgical Tape 1527-2 (3M Health Care, St Paul, Min), which was the state to have a comparable surface roughness ($R_a = 31.5$ μm) and wettability to the human tongue [27]. A half-ring rheometry was utilized to provide the refill of material between the two solid surfaces. The tape was cut in a square form and compacted tightly on top of the lower plate rheometry. After each measurement, the tape was replaced and the instrument was cleaned with deionized water. The extent of 3D printed samples was sufficient to cover the surface of the substrate offered a thin film. For each measurement, the sample (1.0 g) with the average particle size of 200 μm was mixed with saliva in a ratio of 1:1 w/w. To mimic the sensory investigation process, a normal force of 2 N was used to denote the adequate normal force employed during the oral processing [28]. Moreover, the oral condition was mimicked at a temperature of 37 °C. Each 3D printed object was pre-sheared at a speed of 0.02 s^{-1} for 2 min, and after that equilibrated for 1 min before each measurement. The human tongue was reported to move at a speed of 200 mm s^{-1} [29]. Therefore, the tribology assay in the current study was within this range. Afterward, the increasing rotational speed ramp was set from 0.01 to 200 mm s^{-1} with the attainment of 25 points per decade. The values of coefficient of friction (*CoF*) were determined as the friction stress (σ_F) proportion to the normal stress (σ_N), described by Eq. (2):

$$\text{CoF} = \sigma_F/\sigma_N = \quad M/F_N \times (r_2 + r_1)/(r_2^2 + r_1^2) \quad (2)$$

where, M is torque (Nm) and F_N is normal force (N), r_1 is ring inner (14.5 mm) and r_2 is the outer radius (16 mm).

Moreover, the coefficient of friction plotted versus the increasing sliding speed as follows:

$$\nu_s = \overline{R} \times \omega \quad (3)$$

Here, ν_s is the sliding speed (mm s^{-1}), $\overline{R}$ is the mean of ring inner and outer radius, and ω is the controlled rotational speed (rad s^{-1}).

2.5. Temporal dominance of sensations (TDS)

2.5.1. Selection of terms and panel instruction and training

Ten assessors (five females and five males, aged: 24–34 years) participated in this study. They were designated based on the guidelines of the ISO 8586:2012 standard [30] and familiar with the sensation of cheese analogue products. Two 1-h preliminary sessions were conducted to define the TDS methodology and the notion of the temporality of sensations, offering the participants the chance to investigate the data collection software and get acquainted with it. The repeatedly stated sensory features were selected and their descriptions to assess them were defined. The nine selected attributes for 3D printed cheese analogues objects were listed as firmness, thickness, creaminess, graininess, mouth-coating, smoothness, chewiness, fattiness aftertaste, and residue aftertaste. Each attribute reference, applied to acquaint the panelists, is shown in Table A-1 in Supplementary materials. The assessors were afterward trained to employ the computerized TDS data capture system (FIZZ v 2.40A) according to the procedure defined by Pineau et al. [31]. The assessors were needed to place the 3D printed samples into their mouth and click on the start button to begin the assessment. At 15 s, they were demanded to swallow the printed objects via a message presented on the screen and continue the assessment once no attribute was perceived. Then, the panelists were trained to click the stop button excluding data acquisition had automatically stopped upon the time of 60 s. The evaluators were afterward requested to recognize the sensory attributes they perceived as dominant while conducting the testing procedure. The evaluators were also informed that they did not have to choose all the attributes in the list and that they could select a similar sensation frequently during the assessment or in contrast to never choose a descriptor as dominant.

2.5.2. Formal assessment

The temporal dominance of sensations (TDS) method was employed to express variances in the dynamic sensory profile of 3D printed cheese analogue variants. The TDS evaluation was performed over three sessions to run three replications. The 3D printed objects (3 × 3) cm^2 were provided to the assessors by the randomized complete block design in a monadic order. The panelists were then offered a list of nine sensations on the computer screen, each related to an unstructured scale anchored from weak to strong. The normalized time was plotted against the dominance rate of each trait at a given point in time (%). Each curve displayed the progress of the dominance rate of an attribute over time [31]. In this sense, FIZZ software (Version 1.9, Biosystems, Counternon, France) was utilized to obtain the TDS plots. To better illustrate, the smoothed TDS curves were plotted using MATLAB software (R2016a,

MathWorks Inc., Natick, Ma). Two lines were displayed on each TDS graph, namely chance- and significance levels to simplify the interpretation of attributes. The chance level signifies the minimum magnitude of a dominance rate that a trait was attained by chance ($1 \times$ (number of attributes)$^{-1}$). The significance level states the least magnitude of a dominance rate of a given trait, which is significantly higher than the chance level ($P < 0.05$) [31]. Additionally, TDS score was also obtained by Eq. (4), which is mean intensity scores weighted by the duration of each selected sensation during the assessment:

$$\text{TDS score} = (\Sigma_{\text{scoring}}\ \text{Intensity} \times \text{Duration}) / (\Sigma_{\text{scoring}}\ \text{Duration}) \quad (4)$$

2.6. Statistical analysis

All instrumental experiments were carried out as triplicate determinations (except textural properties, in which eight replications were used), and the mean and standard deviation of the data were reported. Analysis of variance (ANOVA) was utilized to determine the main effects of the examined independent factors and their interactions on the instrumental and sensory data. Duncan's multiple range test was applied to separate means of data when significant differences ($P < 0.05$) were observed. Principal component analysis (PCA) was conducted through Unscrambler (Version 9.2, CAMO A/S, Oslo, Norway) to identify the clusters in a data population to visualize the main variation in the data with the principal components (PCs). The obtained score plot, where all objects are plotted according to the new coordinates from the transformed data, allows to easily deduce the main differences in the data set, and clusters of the samples are frequently obvious by the first few PCs. A corresponding plot of variables, correlation loading plot, shows the correlations between the different variables.

3. Results and discussion

3.1. Printing performance

One of the objectives of this work was to produce printable inks, which could be printed with high printing precision, improved resolution of the deposited layers, and shape stability after printing. The printing performance offers a quantitative basis to assess and quality control of printed objects. To evaluate the effect of micro-biosurfactant ratios on the printing performance of casein-based emulsion, the inks with different AMCC contents were printed through layer-by-layer

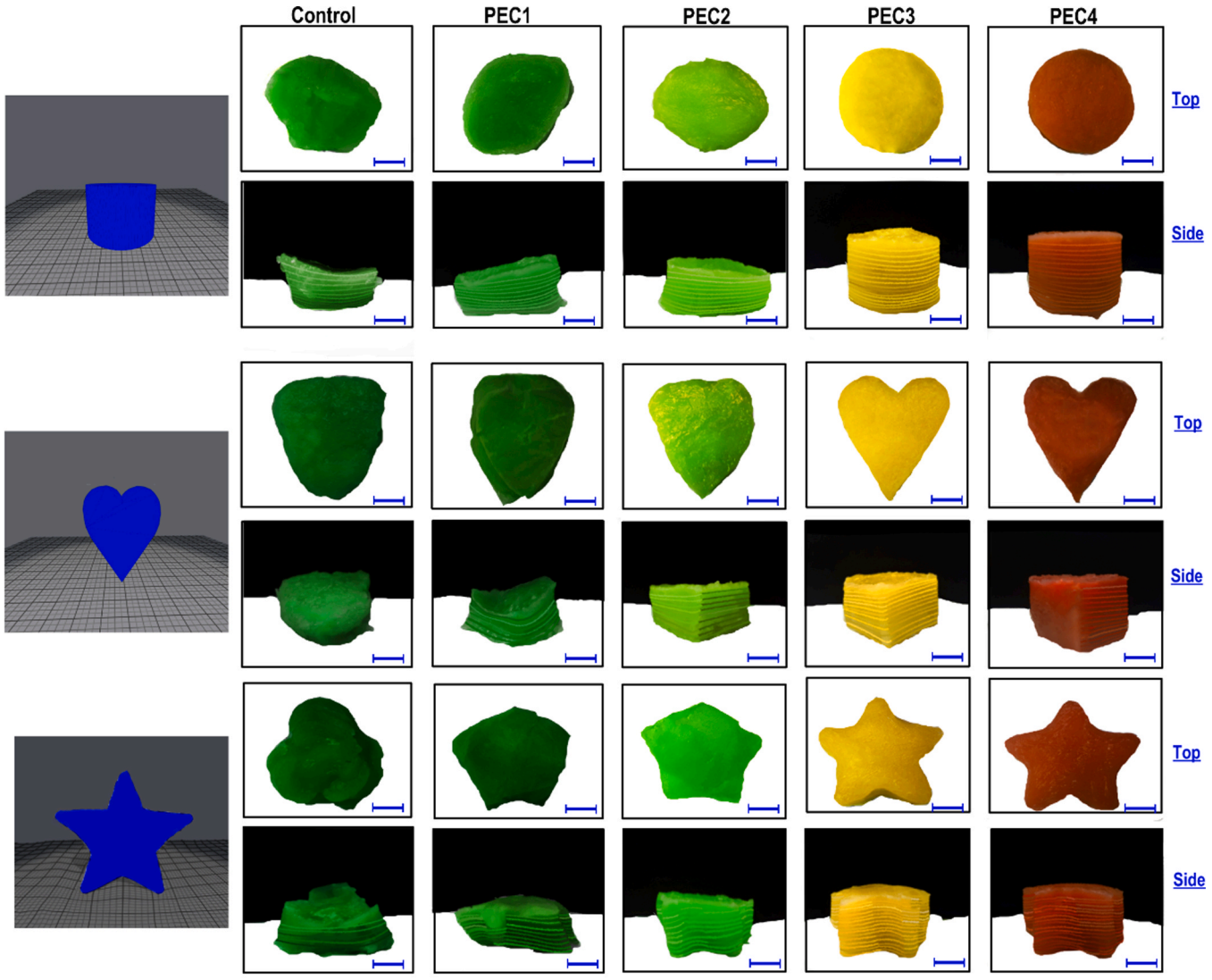

Fig. 1. The cylindrical, heart and star-shaped 3D printed cheese analogue architectures prepared by different ratios of AMCC. The bar scale is 2 cm.

deposition and the resulting images are depicted in Fig. 1.

All the inks containing micro-biosurfactant could be easily extruded out from the nozzle tip. This result was expected since the reduced-fat inks offered a low flow behavior index as shown in Part I of this series [10], where the inks became more shear-thinning with an increase in the level of AMCC. It was stated that higher *pseudoplasticity*, reflected by the lower flow behavior index, would create ease in the extrusion process [2]. As Fig. 1 illustrated, the printed control (and also PEC1) object deformed in time because of sagging (after 5 min), hence displayed poor resolution and weak shape-fidelity as found in different 3D shapes of the star, heart, and cylindrical. In contrast, the addition of AMCC in the casein/oil system was detected to have a positive impact on the printing performance. In this context, the micro-biosurfactant provided the 3D printed structures with a clear and smooth boundary, especially when AMCC at the ratios of 3.15 and 4.2 wt% were added to the formulation (Fig. 1). This result may be due to a better structural strength of PEC3 and PEC4 inks, contributing to the formation of a strong gel-like network (i.e., higher elastic modulus, greater viscosity recovery, strong thixotropic feature, and larger nonlinear elastic character) as reported in Part I of this series [10].

The layer number and line width of printed constructs for each 3D shape are summarized in Table 2, representing the structural strength and printing accuracy, respectively [1]. The line widths and layer numbers of printed PEC1 were found to be similar to the printed control ($P > 0.05$) (Table 2). In contrast, the addition of higher AMCC contents to the ink formulation provided the printed structures with greater layer numbers and thinner line width, indicating better stability and precise geometry. The development of well-defined architectures regarding printed PEC3 and PEC4 could be ascribed to the excellent structural stability and increased extent of nonlinear behavior under large deformations as shown in Part I of this series [10]. It was also reported that the presence of 3.15 and 4.2 wt% AMCCs in the ink formulation increased the complex modulus and improved the thixotropic behavior, enhancing the resistance to the prompt shear stress and deformation [10]. This led to the reinforced spatial resolution of deposited layers in the printed structures.

The appearance of printed architectures can affect consumer acceptability in the market [32]. In this sense, the optical characteristic was taken into account to measure the changes in the color parameters of printed samples (see Supplementary materials for more insight into the optical test investigation of printed architectures). The Hunter Lab color parameters (L^*, a^*, and b^*) and total color difference (ΔE) of 3D printed variants were obtained and data are given in Table 2. The optical data revealed that there was no significant difference concerning color parameters of printed control and PEC1 ($P > 0.05$). The measured Hunter parameters of L^*, a^*, and b^* for these printed samples were approximately determined to be 44, − 34, and − 2, respectively, where L^*, a^*, and b^* are the lightness, red-green coordinate, and yellow-blue coordinate, respectively. The apparent color of printed control was changed from green to the yellowish-green after incorporation of 2.1 wt % micro-biosurfactant (PEC2), which could be simply observed by the naked eye (Fig. 1). In this case, a^* index was, however, not significantly different from printed control and PEC1 ($P > 0.05$). The greater ΔE value of printed PEC2 was a result of increasing the lightness and b^* parameters (Table 2), which might be an indicator of the oil reduction and formation of intermolecular interactions upon micro-biosurfactant incorporation. On the other hand, the initial color parameters were substantially affected after incorporation of 3.15 and 4.2 wt% AMCCs. In this regard, the ΔE values of printed PEC3 and PEC4 were determined to be 19.32 and 16.61, respectively. This outcome could be generally owing to the development of yellow and red colors, resulting from the incorporation of higher amounts of micro-biosurfactant along with reducing a greater level of the oil phase.

3.2. Microstructure evaluations

The VP-SEM micrographs of 3D printed cheese analogues formulated with different ratios of AMCC are schematically presented in Fig. 2 (row i). The micrographs demonstrated there is no protein aggregation in the matrix likely on account of homogeneously dispersed casein upon by the 3D printing process. The printed control sample (column i) was characterized by a compact structure, typically contained casein matrix with many dispersed free-fat globules. The fat globules with a variable size were distributed in the casein matrix, showing minimal inter-particle spaces. In this case, some of the fat globules were specified with fairly round shapes, whose diameters ranged from ~ 10 to 40 μm. In the case of reduced-fat printed samples, it seems the casein developed a more continuous network, whereas the fat globules were placed in the channels throughout the matrix. Moreover, there was an increased number of pores, which showed a more open structure (Fig. 2 columns ii-iv), possibly caused by reduction of the oil phase and presence of micro-biosurfactant. This was more the case for 3D printed objects with higher micro-biosurfactant contents, i.e., PEC3 and PEC4. Generally, the microstructure of printed PEC1 (not shown) and PEC2 was comparable, in which there were some low-level pores in the protein bulk, which were also filled with the free-fat globules in the system. Furthermore, their matrix presented a comparatively uneven and rough structure compared to printed PEC3 and PEC4. Due to the irregular distribution of fat compounds, the size of the pore in printed PEC1 and PEC2 was different. In contrast, with increasing micro-biosurfactant ratio, the structure of printed PEC3 and PEC4 shifted to a more uniform matrix, where the amounts of free-fat globules progressively decreased and the number of pore structures increased (Fig. 2 columns iii and iv). Additionally, the printed PEC3 and PEC4 obviously presented a denser microstructure compared to the other printed samples. The observed differences in the microstructure of the 3D printed objects might be related to differences in the rheological properties and structural stability of their ink counterparts [10]. A certain degree of interaction between the hydrophobic and hydrophilic domains of acetylated MCC with functional groups of oil and casein, respectively, could lead to the development of a more compact structure.

Fig. 2 also displays the location and distribution of the fat globules inside the printed bulk casein detected by CLSM (row ii). As depicted, the casein was obviously visible through CLSM as a green/bright green color and homogeneously distributed throughout the system. Regarding printed control, a high level of free-fat phase with a large size (red color)

Table 2
Summary of the line widths and layer numbers, as well as Hunter Lab color parameters of 3D printed cheese analogues variants.

Sample	Cylindrical		Heart		Star		Optical characteristic			
	Line width (mm)	Layer numbers	Line width (mm)	Layer numbers	Line width (mm)	Layer numbers	L*	a*	b*	ΔE
Control	3.9 ± 0.1^{c}	9 ± 1^{a}	5.4 ± 0.3^{d}	7 ± 1^{a}	4.9 ± 0.3^{e}	8 ± 1^{a}	44.1 ± 1.8^{a}	-34.2 ± 1.6^{a}	-1.9 ± 0.01^{a}	–
PEC1	3.7 ± 0.2^{bc}	10 ± 1^{a}	4.9 ± 0.4^{cd}	7 ± 2^{a}	4.2 ± 0.3^{d}	9 ± 2^{a}	44.6 ± 1.5^{a}	-34.0 ± 1.8^{a}	-2 ± 0.01^{a}	0.29
PEC2	3.2 ± 0.4^{b}	12 ± 1^{b}	4.6 ± 0.3^{c}	12 ± 2^{b}	3.6 ± 0.2^{c}	14 ± 1^{b}	56.4 ± 1.2^{c}	-31.2 ± 1.5^{a}	13.9 ± 0.4^{b}	10.10
PEC3	1.9 ± 0.03^{a}	24 ± 2^{c}	1.3 ± 0.01^{b}	20 ± 1^{c}	1.2 ± 0.01^{b}	21 ± 2^{c}	68.3 ± 1.5^{d}	-6.8 ± 0.2^{b}	44.9 ± 1.6^{d}	19.32
PEC4	1.9 ± 0.05^{a}	26 ± 1^{c}	1.0 ± 0.01^{a}	22 ± 2^{c}	0.9 ± 0.01^{a}	24 ± 2^{c}	47.3 ± 1.3^{b}	36.4 ± 1.0^{c}	27.2 ± 0.8^{c}	16.61

[a–e] Means inside each column with different letters are significantly different ($P < 0.05$), Duncan's test.

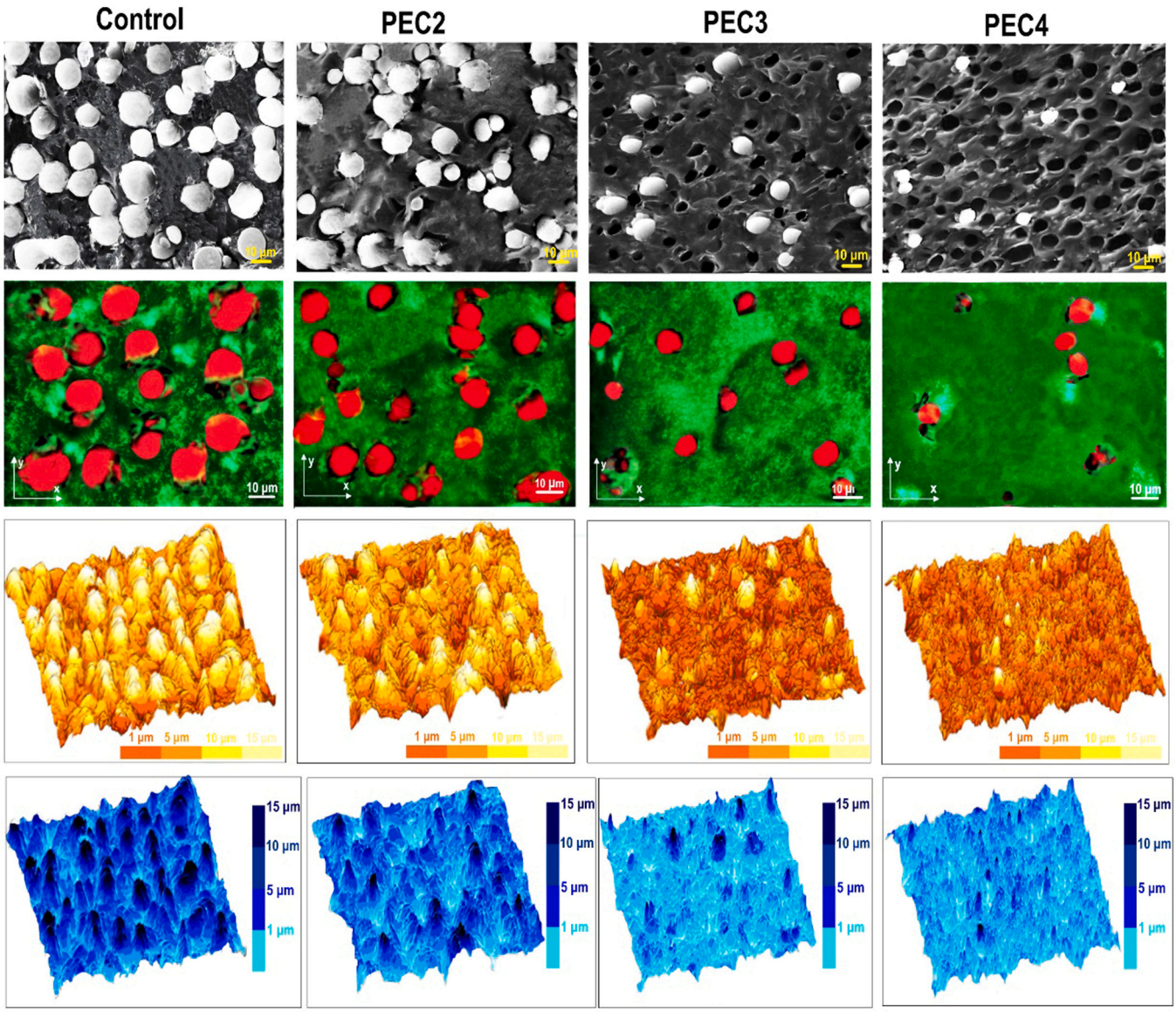

Fig. 2. The VP-SEM photomicrographs of 3D printed cheese analogues formulated by different ratios of micro-biosurfactant (row i). The CLSM images of 3D printed objects where oil phase and casein matrix are stained as red and green/bright green color, respectively (row ii). The typical 3D AFM (row iii) and high-resolution AFM (row iv) topography images of 3D printed variants.

was evident in the bulk, which was possibly related to the absence of micro-biosurfactant. Similarly, printed PEC1 (not shown) and PEC2, which contained 1.05 and 2.1 wt% AMCC, respectively, did not show major microstructural changes compared to printed control, whose microstructures were almost similar. In these cases, however, an even smaller level of dispersed free-fat globules within the matrix could be observed. On the contrary, the CLSM images of printed PEC3 and PEC4 seem quite different in structure. As expected, they showed a low level of fat globules in the matrix. This was not surprising, since most of the oil was replaced with micro-biosurfactant. Besides, the higher ratios of AMCC also led to a reduction of fat globules size. This result agreed with the particle size distribution reported in Part I of this series, in which the particle size of Pickering emulsion containing micro-biosurfactant underwent a substantial reduction [10]. Owing to the importance of biopolymeric surfactant for the stabilization of the droplets/particles in the fat-based food dispersions, the acetylated MCC could contribute to the emulsion stability against phase separation, where the dispersion was free from any strong (irreversible) flocculation and coalescence.

Fig. 2 also shows the topographic micrographs of 3D AFM (row iii) and high-resolution AFM (row iv). On this subject, the average roughness (R_a) and root-mean square roughness (R_q) of printed cheese analogue variants were also analyzed and data are summarized in Table 3. The R_a shows the average of the absolute extent of height deviations from the mean surface, and R_q expresses the magnitude of the root-mean square average of height deviations from the mean plane [33]. As Fig. 2 depicted, the surface topography of printed control showed an uneven matrix with many pits and hills on its surface, whose R_a and R_q values were measured to be 46.1 µm and 56.2 µm, respectively (Table 3). The topographic image of printed control also presented a limited space and fewer crevices with the lower inter-particle network spaces. This minimal inter-particle space and bumpy matrix could be related to the presence of a large number of free-fat globules on the surface of printed control owing to the lack of used micro-biosurfactant in its formulation. This result was supported by VP-SEM and CLSM micrographs. Likewise, the topographic images of printed PEC1 (not shown) and PEC2 also presented a high level of irregularity with several micro-sized particles on their surface, offering high roughness parameters (Table 3). As presented in Fig. 2, the changes in the topographies of

Table 3
Summary of topological variables detected by AFM and textural parameters obtained by TPA of 3D printed cheese variants.

Sample	AFM parameters		TPA parameters				
	R_a*(μm)	R_q** (μm)	Hardness (N)	Cohesiveness	Gumminess (N)	Springiness (mm)	Chewiness (N mm)
Control	46.1 ± 0.7^{e}	56.2 ± 0.5^{d}	22.4 ± 0.4^{a}	0.34 ± 0.02^{a}	7.62 ± 0.31^{a}	4.2 ± 0.2^{a}	32.0 ± 2.2^{a}
PEC1	43.3 ± 0.6^{d}	54.9 ± 0.6^{d}	21.8 ± 0.6^{a}	0.34 ± 0.02^{a}	7.41 ± 0.20^{a}	4.3 ± 0.4^{a}	31.8 ± 2.4^{a}
PEC2	39.6 ± 0.7^{c}	44.4 ± 0.7^{c}	25.3 ± 0.7^{b}	0.36 ± 0.03^{a}	9.11 ± 0.36^{b}	4.3 ± 0.6^{a}	39.1 ± 1.8^{b}
PEC3	17.7 ± 0.1^{b}	23.5 ± 0.3^{b}	47.8 ± 0.6^{c}	0.78 ± 0.03^{b}	37.28 ± 1.12^{c}	4.3 ± 0.3^{a}	160.3 ± 7.4^{c}
PEC4	9.4 ± 0.1^{a}	18.7 ± 0.4^{a}	46.4 ± 0.8^{c}	0.88 ± 0.03^{c}	40.83 ± 0.94^{d}	4.9 ± 0.2^{b}	200.0 ± 10.3^{d}

[a–e] Means inside each column with different letters are significantly different ($P < 0.05$), Duncan's test.
*R_a: Average roughness.
**Rq: Root-mean-square roughness.

printed PEC3 and PEC4 were specified by a surface smoothing, providing a network with a lower surface roughness (Table 3). This presented an almost uniform and homogeneous structure with the areas of free slits and cracks. The desired surface topology in the microstructure of printed PEC3 and PEC4 was expected as the higher ratios of micro-biosurfactant effectively contributed to the surface coating of the oil droplets dispersed in the casein phase [10]. The obtained microstructure outcomes were also consistent with the results of printing performance. As a consequence, the application of different morphological experiments to evaluate the microstructure of 3D printed objects offered a piece of valuable information in determining the distribution of fat globules in the reduced-fat products. This would then provide a sensitive analytical tool in future studies to observe the specific components within the 3D structures.

3.3. Textural properties

The texture is considered a critical parameter determining the quality of 3D printed products [3]. It is strongly related to the mouthfeel of food that critically affects the consumers' acceptability. Table 3 shows the textural parameters of 3D printed cheese analogue variants measured by TPA assay. The printed control presented a soft texture with a hardness value of 22.4 N. According to the TPA results, the addition of AMCC showed a significant hardening effect on the system ($P < 0.05$), though the micro-biosurfactant at the ratio of 1.05 wt% did not induce a significant change in the hardness parameter ($P > 0.05$). As can be seen in Table 3, the hardness value was appreciably increased by 11.5%, 113.4%, and 107.1% regarding printed PEC2, PEC3, and PEC4, respectively. The hardening effect of AMCC, especially at the higher contents, could be assigned to the greater elastic modulus, larger yield stress, and increased nonlinear oscillatory response induced in the casein-based ink as stated in Part I of this series [10]. The presence of more amphiphilic groups in the system may offer strong intermolecular interactions between acetyl and hydrophilic groups of AMCC with oil and casein, respectively. This consequently led to the formation of a rigid structure. The textural data also showed the printed control and PEC1 displayed a less cohesive matrix compared to other printed samples with a value of 0.34 (Table 3). The cohesiveness value of printed PEC2 was also significantly remained similar to that value obtained for printed control ($P > 0.05$). In contrast, an obvious increase in the cohesiveness parameter was detected when AMCC at a ratio of 3.15 and 4.2 wt% was introduced into the system. This change was probably assigned to the development of a thixotropic system with a reversible matrix regarding PEC3 and PEC4 inks [10]. This may lead to the development of a cohesive texture and offering a system with higher strength of internal linkages.

The gumminess parameter signifies the extent of work required to produce a 3D printed object ready to swallow. In this case, 3D printed PEC3 and PEC4 constructs showed remarkably higher gumminess values, followed by printed PEC2, which in turn, printed control and PEC1 presented the lowest gumminess value (Table 3). In this context, the initial gumminess amount was increased by 19.5%, 389.2%, and 435.8% regarding printed PEC2, PEC3, and PEC4, respectively. The greater gumminess value obtained by higher levels of micro-biosurfactant might be thanks to the formation of a dense matrix with a more reversible structure in the printable ink counterparts [10]. The textural data also exposed that the initial chewiness value was more increased by about 22%, 400%, and 525% when AMCC at a level of 2.1, 3.15, and 4.2 wt% was added to the formulation, respectively. As a consequence, the printed PEC3 and PEC4 were considerably harder, more cohesive, and more chewable than the other printed samples. This could be reflected by the promotion of a well-defined gel-like network with a structured system in their ink counterparts. As discussed in Part I of this series, a greater AMCC ratio offered an ink with higher structural strength, larger critical strain, and increased nonlinear oscillatory response [10]. This led to the progress of more intermolecular junctions in the system and reinforcement of the network extension through the steric and/or electrostatic repulsive interactions, which consequently improved the mechanical properties.

3.4. Thermal behavior

The freeze-thaw stability is an imperative feature to evaluate the ability of food products to withstand the unfavorable physical changes during storage that can happen upon freezing and thawing [34]. As depicted in the thermogram of 3D printed control (Fig. 3a), three endothermic peaks were distinguished in the DSC heating curve, which was also detected in all reduced-fat printed objects. In the heating curve of printed control, the first endothermic peak was responsible for the fat melting phenomenon and ranged from − 32.2 to − 9.4 °C with a melting point (T_m) of about − 19.5 °C. The obtained values are in correspondence with data reported by dos Santos et al. [35] for canola oil. It should be noted that the sharp peak of fat melting shows nearly all of the triglycerides melted in a narrow temperature range. The second peak with T_m of about − 1.6 °C was attributed to the ice melting in the printed control. Finally, the endothermic peak ranged from 94.3 to 112.1 °C could be ascribed to the water evaporation, whose midpoint temperature was obtained to be 102.4 °C. The changes in the thermal parameters of the 3D printed casein/oil system as affected by AMCC incorporation are also schematically presented in Fig. 3a. It could be found that replacement of oil by micro-biosurfactant caused a considerable shift of the fat melting point to the higher temperatures, except for printed PEC1. Similarly, the T_m values of the ice melting and water evaporation were obviously moved to the higher temperature, especially in the printed samples with the higher AMCC ratios. These observations showed that the oil/aqueous phases were strongly involved with hydrophobic/hydrophilic groups of micro-biosurfactant, which offered a higher temperature for fat melting/ice melting/water evaporation. Then, the intermolecular interactions could effectively bind the oil/-water molecules and as a result, developed a strong gel-like network, leading to blocked or reduced available oil and water in the system.

On the other side, the peak areas (enthalpy) of the first endothermic event became smaller when oil was replaced by micro-biosurfactant (Fig. 3a). This was more obvious especially in the case of printed

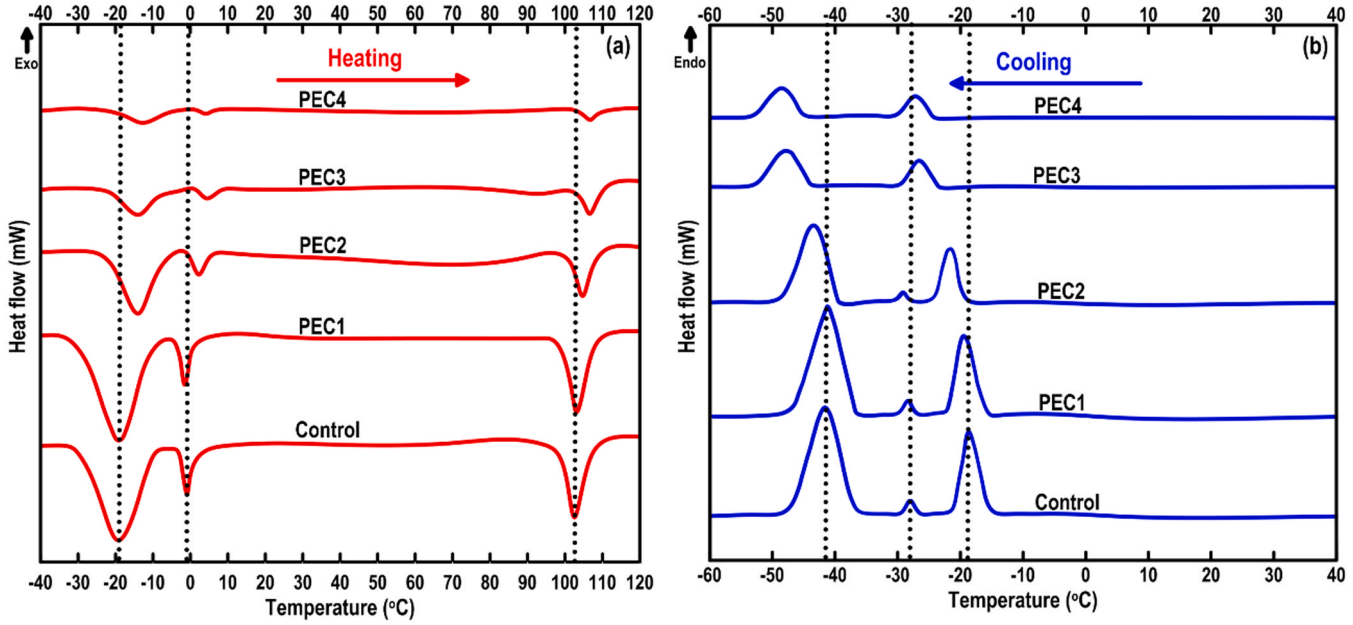

Fig. 3. The obtained DSC thermograms of 3D printed cheese analogue variants. (a): DSC heating curves and (b): DSC cooling analysis. The heating rate was 10 °C min^{-1}.

PEC3 and PEC4. The reduced enthalpy of endothermic behaviors upon AMCC replacement could be also generalized to the melting ice and water evaporation peaks. It should note that when 1.05 wt% AMCC was added to the formulation (i.e., PEC1), the peak areas of the endothermic behaviors did not change and remained similar to the printed control. The enthalpy reduction caused by micro-biosurfactant incorporation might be attributed to the interactions of hydroxyl/carboxyl and acetyl groups of AMCC with water and oil, respectively, thereby decreasing the amount of free oil and water in the system. Besides, it should be borne in mind that the reduced peak area of fat could be also assigned to the lesser amount of oil phase where some of the oil was replaced by AMCC.

The food products are generally needed to be frozen before consumption, either for product preservation, particularly to prevent the chemical degradation reactions and microbial growth, or for product preparation [34]. As shown in Fig. 3b, the DSC cooling analysis of 3D printed control presented the exothermic peaks of water crystallization peak (Tc_{water}) at about − 19.2 °C and oil crystallization (Tc_{oil}) at − 28.2 °C and − 42.6 °C. The presence of two peaks regarding the oil crystallization was most probably because the canola oil was a complex mixture of triglycerides that crystallized as two independent portions of high- and low-melting triglycerides [36]. In the DSC cooling behavior of the reduced-fat printed samples, there was a decreasing trend in the peak areas of the exothermic event. Once again, the thermogram of printed PEC1 remained similar to the printed control (Fig. 3b). It is interesting to note that the addition of 3.15 and 4.2 wt% AMCC ratios to the formulation led to the disappearance of the first oil crystallization (located at about −28.2 °C). This outcome might be attributed to the existence of strong intermolecular interactions between the acetyl groups of micro-biosurfactant and hydrophobic domains of oil fraction, promoting a more structured system with a strong gel-like network. Among the reduced-fat 3D printed samples, the lowest freezing peak temperature was observed for printed PEC3 and PEC4. In this regard, both printed PEC3 and PEC4 exhibited a comparable DSC profile with Tc_{water} and Tc_{oil} of around − 26 and − 48 °C, respectively. The observations indicated that the oil and aqueous phases in these systems were less readily frozen than those of other printed samples. The greater stability of printed PEC3 and PEC4 against freezing could be, to a large extent, associated with the existence of the higher levels of surface-active biopolymer, enabling them to make strong intermolecular interactions. It was shown that AMCC is very effective to promote steric stabilization and/or electrostatic repulsive interactions on account of the presence of multiple binding sites at the interface [10]. Then, it could be argued that the AMCC has an oil- and water-binding effect, resulting in the reduction of free oil/water phases in the system.

3.5. Crystalline pattern

The XRD analysis was conducted to determine the change in the crystalline structure of the 3D printed cheese analogue upon micro-biosurfactant addition (Fig. 4). The diffractogram of AMCC showed a crystalline structure with the strong reflections at $2\theta = 14.5°$, $2\theta = 23.2°$, and $2\theta = 35.1°$, presenting the dominance of the cellulose type I in the acetylated MCC [12]. The total relative crystallinity degree (RCD) of AMCC was also obtained about 76% that was rather lower than the crystallinity index of 84% detected by ^{13}C NMR, measuring in Part I of this series [10]. The XRD pattern of the pristine casein used in this study also presented a typical crystalline structure with principally two pronounced diffraction peaks locating at around $2\theta = 9.5°$ and $2\theta = 20°$ with a total relative crystallinity of 28.4% (Fig. 4). The diffractogram of 3D printed samples showed the manufacture of Pickering emulsion along with the application of printing process led to a weakening of the pronounced peaks of casein locating at $2\theta = 9.5°$ and $2\theta = 20°$. This signified a slight chain degradation occurred in the inter-helical structure of 3D printed samples [19]. In this sense, XRD patterns of printed control and PEC1 revealed the characteristic peaks of pristine casein were transformed into the diffused peaks, representing a loss in crystallinity upon the 3D printing process. The RCD of these samples was also dropped to a value of about 17.5%. This could be due to a decrease in the intensity of crystalline reflections of the main casein diffraction peaks. As Fig. 4 shown, the intensity of pronounced peaks of casein was more declined regarding printed samples formulated with higher AMCC ratios. In this context, a notable decrease in the RCD to 15.1%, 8.3%, and 7.6% was found concerning 3D printed PEC2, PEC3, and PEC4, respectively. On this subject, the characteristic peak of casein located at about $2\theta = 20°$ changed to a broader and flatter pattern regarding printed PEC3 and PEC4, offering an amorphous-like state. This might be attributed to the conversion of the casein crystalline domains to the amorphous state by losing its crystallinity. This outcome was supported

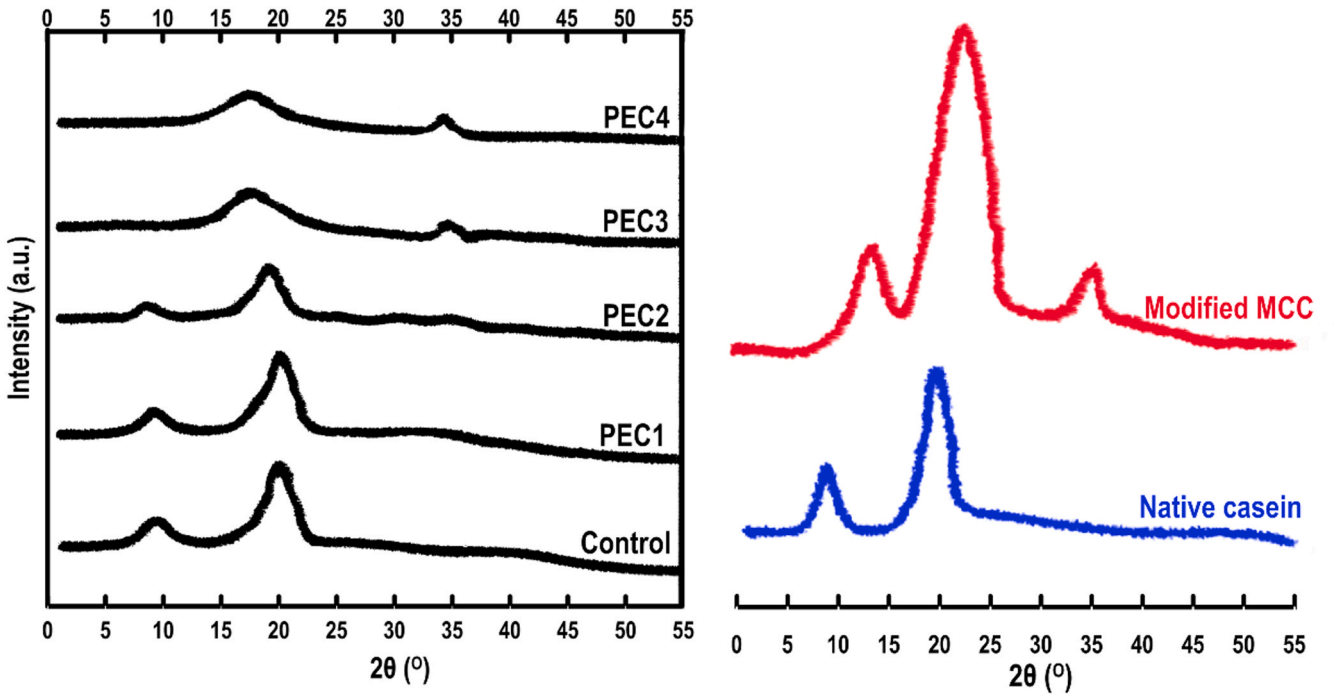

Fig. 4. The XRD patterns of 3D printed cheese analogue variants **(left)**. The diffractograms of acetylated MCC and pristine casein **(right)**.

by DSC results, where the strong interactions among polar groups of AMCC and casein could notably reduce the crystalline regions of the matrix. It is necessary to add a new minor reflection at about $2\theta = 35°$ was emerged in the diffractograms of printed PEC3 and PEC4, assigning to the pronounced peak of AMCC (Fig. 4). However, there was no new peak appearing in the XRD patterns of 3D printed PEC1 and PEC2. This means that AMCC at the levels of 1.05 and 2.1 wt% could not induce new crystalloid in the polymeric structure.

The average distance between the layers (interlayer d_{001} spacing) for 3D printed control and PEC1 was also obtained to be $d_{001} = 8.3$ Å ($2\theta = 9.5°$) and $d_{001} = 6.1$ Å ($2\theta = 20°$). Regarding 3D printed cheese analogue fabricated by 2.1 wt% AMCC (i.e., PEC2), the characteristic peak of casein from $2\theta = 20°$ slightly moved to $2\theta = 19.1°$, which specified that the gallery spacing from $d_{001} = 6.1$ Å ($2\theta = 20°$) increased to $d_{001} = 6.6$ Å ($2\theta = 19.1°$). The shift to the lower angle shows an increase in the corresponding interlayer spacing, which implies the material has a less ordered structure with a decreased chain mobility [37]. This result specified that the interaction of hydrophilic groups of micro-biosurfactant (at the level of 2.1 wt%) with casein, to some extent, led to the changes of spatial structure and unfolding of casein. A more shift to the lower 2θ values was obtained after the manufacture of printed PEC3 and PEC4, corresponding to an increase in the gallery spacing to $d_{001} = 7.4$ Å ($2\theta = 17.3°$). This indicated a hinder in the chain segment motion with a huge redistribution of the basic crystal lattice and losing the system crystallinity. These results might be ascribed to the strong interaction of carboxyl and hydroxyl groups of

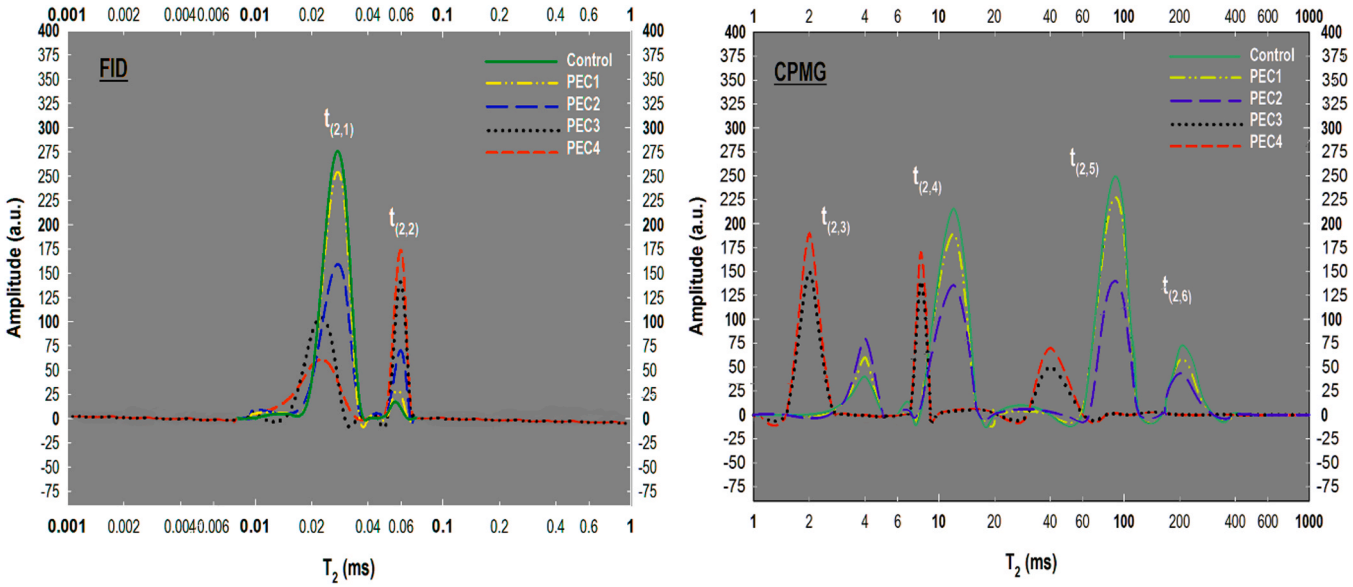

Fig. 5. Proton distributions of the 3D printed cheese analogues obtained by inverse Laplace transformation of the single pulse-free induction decay (FID) and decay obtained with the Carr-Purcell-Meiboom-Gill pulse sequence (CPMG).

Table 4
The T_2 relaxation time of signal amplitude of protons detected by low-field ^{1}H NMR.

Samples	$t_{(2,1)}$ (ms) × 10^{-3}	$t_{(2,2)}$ (ms) × 10^{-3}	$t_{(2,3)}$ (ms)	$t_{(2,4)}$ (ms)	$t_{(2,5)}$ (ms)	$t_{(2,6)}$ (ms)
Control	31 ± 4^{b}	59 ± 2^{b}	4.01 ± 0.3^{b}	12.46 ± 0.1^{b}	96.03 ± 1.7^{b}	196.26 ± 3^{a}
PEC1	31 ± 6^{b}	59 ± 2^{b}	4.02 ± 0.3^{b}	12.44 ± 0.2^{b}	95.33 ± 1.9^{b}	195.31 ± 4^{a}
PEC2	33 ± 7^{b}	60 ± 4^{b}	4.03 ± 0.3^{b}	12.53 ± 0.3^{b}	96.15 ± 1.7^{b}	194.11 ± 3^{a}
PEC3	25 ± 4^{a}	57 ± 3^{a}	2.02 ± 0.3^{a}	8.39 ± 0.1^{a}	40.37 ± 0.8^{a}	Nd*
PEC4	25 ± 6^{a}	57 ± 4^{a}	2.03 ± 0.2^{a}	8.42 ± 0.1^{a}	40.33 ± 1.0^{a}	nd

$^{a–e}$ Values are the average of triplicates ± standard deviation. Different superscripts in each column show a significant statistical difference ($P < 0.05$).
*nd: not detected.

AMCC through hydrogen bonding with casein offered by introducing a higher micro-biosurfactant ratio. These interactions could decrease the inter- and intramolecular linkages between the casein chains, and consequently disordering of the biopolymeric domains.

3.6. Proton mobility by TD NMR spectroscopy

The TD NMR has been recognized to be a fast, reproducible, and non-invasive method aimed at the measurement of proton mobility [38]. It provides a good estimate for the molecular interaction of water and oil with other biopolymers and macroscopic properties including changes in crystallinity and hardness. The FID and CPMG proton distribution patterns of the 3D printed cheese analogue variants are illustrated in Fig. 5. There are two separate FID and four distinct CPMG proton populations in each 3D printed variant, denoting as $t_{(2,1)}$, $t_{(2,2)}$, $t_{(2,3)}$, $t_{(2,4)}$, $t_{(2,5)}$, and $t_{(2,6)}$ populations. From Fig. 5, there are also two abundant proton populations in the FID and CPMG distribution curves. The prevailing $t_{(2,1)}$ population, which emerged in the FID spectrum, could be included the non-exchanging protons that were not in contact with water [24]. This dominant population also offered the lowest mobility (Table 4). Based on the literature, the $t_{(2,1)}$ population primarily comprises the CH protons of tightly packed casein crystals, rigid CH protons of the solid fat crystals, and also rigid non-exchanging protons of AMCC crystal (except printed control) that are not subjected to water [39]. The next prevailing proton population (i.e., $t_{(2,5)}$ population), recognized in the CPMG distribution curve, was considered as a more mobile environment. This population can be attributed to the mobile hydroxyl protons of casein in strong association with water [39]. Regarding reduced-fat 3D printed objects, this panel also included the water protons enclosing AMCC in the exchange for their protons. On the other hand, the $t_{(2,2)}$ (in FID spectrum) and $t_{(2,3)}$ (in CPMG sequence) populations could be related to the CH protons of amorphous regions of casein and AMCC with limited interaction with the confined water [24]. The $t_{(2,4)}$ panel allocated to the OH protons of casein and water in a less mobile environment. Moreover, some CH protons of casein and confined water could also be included [24]. In the cased of reduced-fat 3D printed objects, it could reasonably be assumed some of the OH and CH protons of AMCC were part of the $t_{(2,4)}$ population. These protons probably were involved with water, presenting more mobility compared to the rigid non-exchanging CH protons that were not exposed to water in the $t_{(2,1)}$ population [38]. Lastly, there were minor relaxation signals in the CPMG distribution curve as $t_{(2,6)}$ population. This relaxation peak was detected principally in the printed control, PEC1, and PEC2, attributing to the protons of free oil in the system [25].

According to the NMR results, the proton distribution pattern of printed control and PEC1 in terms of resolution of FID and CPMG curves and relaxation time of the populations was comparable. The higher amplitude of the $t_{(2,1)}$ population regarding printed control and PEC1 may be associated with a greater amount of the non-exchanging protons, which led to an increase in the CH protons in the rigid domains that were not exposed to water. As Fig. 5 depicted, the replacement of oil by the higher micro-biosurfactant ratios in the printed PEC2, PEC3, and PEC4 induced a huge reduction in the amplitude of $t_{(2,1)}$ population. This was more obvious when AMCC at levels 3.15 and 4.2 wt% was added to the formulation. The lower amplitude of the $t_{(2,1)}$ population could be ascribed to the lower amount of solid crystals, representing a reduction in the tightly bound water. This change led to a decrease of CH protons that are not exposed to water in the rigid domain, which resulted in an increased amorphous region [24]. It was described that there is a linear relationship between the amplitude of panel $t_{(2,1)}$ and crystallinity [24, 39]. As discussed in DSC and XRD sections, incorporation of AMCC reduced the crystallinity of 3D printed objects due to the formation of strong interaction between carboxyl/hydroxyl groups of AMCC with comparable groups of casein through hydrogen bonding. This interaction produced the disordered chains by the formation of inter- and intramolecular linkages between the casein matrix and subsequently leading to a smaller amplitude of $t_{(2,1)}$ population.

On the other hand, the increased amplitude of $t_{(2,2)}$ and $t_{(2,3)}$ populations concerning printed PEC2, PEC3, and PEC4 over control and PEC1 was caused by the increased fractions of more mobile protons of casein and also AMCC that are in little association with water. These changes could be mainly ascribed to (*i*): a reduction of the solid proton crystals that were not subjected to water (i.e., $t_{(2,1)}$ panel), and (*ii*): a rise in the amorphous protons in little contact with the confined water (i.e., $t_{(2,2)}$ and $t_{(2,3)}$ panels). At the same time, the characteristic $t_{(2,5)}$ population (in the CPMG spectrum) of printed PEC2, PEC3, and PEC4 was greatly reduced compared to printed control and PEC1. This suggested that the incorporation of higher ratios of micro-biosurfactant induced a strong water-binding property. Additionally, the absence of $t_{(2,6)}$ relaxation peak concerning printed PEC3 and PEC4 could be ascribed to the reduced fractions of more mobile oil. This change might be due to the increased interactions among the acetylated groups of AMCC with the oil portion and the presence of the less mobile environment as more hydrophobic portions of AMCC were interacted with the free oil in the system. These results were supported by the XRD crystallography and also DSC experiments.

Concerning the T_2 (spin-spin) relaxation time, the oil replacement with micro-biosurfactant induced obvious alterations in the relaxation time of 3D printed samples. As given in Table 4, the T_2 relaxation time of the population $t_{(2,1)}$ (and also $t_{(2,2)}$) in the FID was significantly shifted to the lower relaxations regarding printed PEC3 and PEC4 ($P < 0.05$). This indicates the fact that the rigid non-exchanging CH protons of casein, solid fat, and AMCC crystals became less mobile and thus, shifted to the shorter T_2 relaxation times. It was reported a shorter FID time is correlated with a high magnitude of hardness [38,39], which is in accordance with the hardness parameter determined by the TPA results. The CPMG sequence also revealed a reduction in the T_2 relaxation times of populations $t_{(2,3)}$-$t_{(2,5)}$ in the printed PEC3 and PEC4. This proposed the ability of higher ratios of micro-biosurfactant to immobilize water in the matrix. The reduced mobility of the population $t_{(2,5)}$ was most probably caused by the strengthening of the 3D printed cheese analogue network on account of the existence of a positive relationship between the hardness parameter and T_2 relaxation time of population $t_{(2,5)}$ [24]. This specified that there were more functional groups available to entrap the mobile protons in the 3D printed objects formulated with the higher AMCC levels, in which they required less time to restore their original spin orientation [25].

3.7. Oral tribology properties

The oral tribological process can be considered valuable for understanding the lubrication behavior in clarifying mechanisms involved in the perception of sensory attributes elicited by printed cheese analogues, which therefore can be assigned to the satiating expectation cues [40]. When food samples are removed from the cavity of the mouth, their residues can support the lubrication, which could be assigned to the sensory attributes such as mouth-coating, creaminess, and fattiness aftertaste. The Stribeck curves (log *CoF* versus log ν_s) are displayed the friction performance of the 3D printed cheese analogues as influenced by AMCC addition and saliva mixing (Fig. 6a and c). It was found that all 3D printed variants showed both boundary and mixed regimes of typical Stribeck curves [41]. The Stribeck curve data indicated that there were small differences between 3D printed constructs in a sliding speed of < 1 mm s^{-1} (Fig. 6a). This result signified that replacing oil with micro-biosurfactant did not show any obvious impact on the tribological feature at the low sliding speed range ($0.01 \leq \nu_s \leq 1$ mm s^{-1}). In these low sliding speeds, recognized as the boundary lubrication regime, the surfaces of the printed objects are in contact that happens once the hydrodynamics can no longer support the load. In this area, the friction is almost constant and mainly governed by the molecular-level interaction and the asperity geometry of the surfaces. As the speed increased ($\nu_s \geq 1$ mm s^{-1}), the samples are entrained into the contact, creating a pressure that supports the separation of the solid surfaces, causing the decreased friction effects [42]. The *CoF* determined in this speed range could be suitable for understanding the potential application of the tribological data in the oral processing, texture, and mouthfeel of products [40]. In this regime, a hydrodynamic film is produced that considerably decreases the friction, where the Stribeck curve comes into the mixed area. Fig. 6a shows the alterations in the lubrication features among the 3D printed objects increased in the mixed regimes. Compared to printed control, the 3D printed PEC1 and PEC2 showed a small decrease in the friction effects, while there was a notable reduction in the *CoF* regarding printed PEC3 and PEC4. The lower *CoF* of these printed samples is a sign of the desired lubrication feature. This proposes that the replacement of oil by the higher levels of micro-biosurfactant improved the tribological feature of 3D printed cheese analogue. The reduction in friction is principally governed by the flow properties that promote fluid entrainment. In this context, the friction coefficient is dominated by the higher total solids content and rheological properties in the contact region [42]. Then, the observed changes between 3D printed variants in the mixed area might be partly described by the higher elastic modulus and increased nonlinear

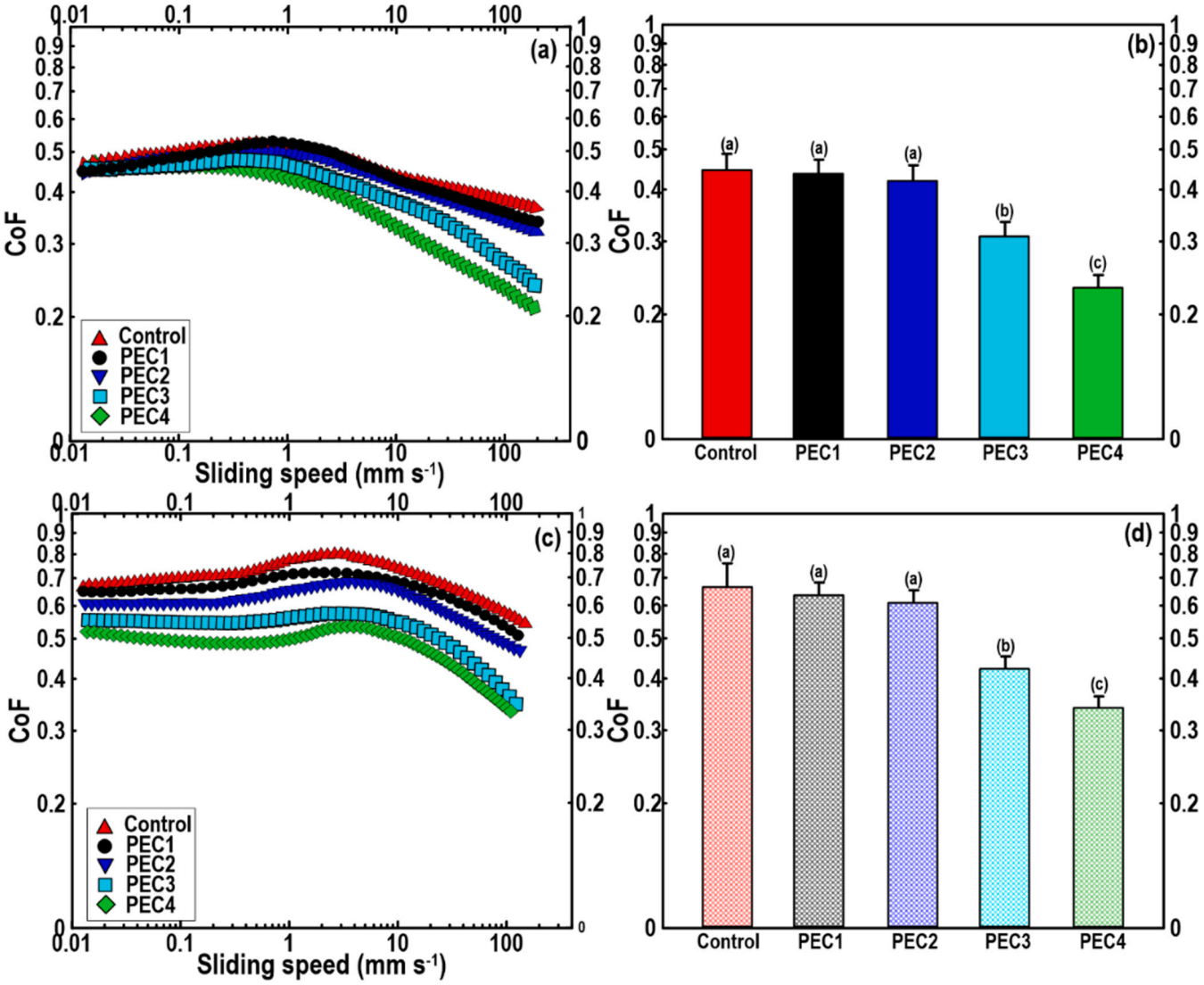

Fig. 6. The friction curves of 3D printed cheese analogues variants without (a) and with saliva (c). The measured coefficient friction of printed samples without (b) and with saliva (d). The means inside each column with different letters (a–c) are significantly different ($P < 0.05$), Duncan's test.

oscillatory response detected in PEC3 and PEC4 inks, reporting in Part I of this series [10]. Furthermore, as PEC3 and PEC4 inks showed a smaller average particle size [10], more particles could enter the contact zone and form a lubricating film on the surfaces. As an additional statement, it has been reported a decrease in the surface roughness and fewer surface irregularities are associated with a lower friction coefficient in the mixed regime [43]. Then, the lower *CoF* offered by the higher micro-biosurfactant ratio was in accordance with the lowered surface roughness measured by AFM assay in the current study.

A key parameter that is often overlooked while evaluating the tribological feature of food systems is the impact of saliva on lubrication and its interaction with the food constituents. The tongue has a hydrophobic nature, and saliva as a natural lubricant can cover the tongue [40]. Then, it might be anticipated to lubricate the hydrophobic 3 M Transpore Surgical Tape surface quite well. Surprisingly, the results in Fig. 6c and d revealed the saliva-containing 3D printed samples gave much higher friction than those of free-saliva ones (Fig. 6a and b). The tribological data showed that when saliva-containing 3D printed objects were sheared between the tested hydrophobic surfaces, the *CoF* value was increased compared to corresponded printed samples without saliva. This is outstanding as saliva alone acts as an appropriate lubricant, which develops the wear-resistant film in the oral cavity via the assembly of small molecular weight proteins layer along with mucins [41]. In this scenario, a lower *CoF* was expected through the key biological lubricant of the mouth, i.e., saliva, presented in the tribological contact. Apparently, the saliva acted like a bulk protein concerning adherence and increasing the *CoF*. Furthermore, the dilution effect of the 3D printed samples with saliva might be another reason for such behavior, as the dilution could induce a reduction in the flow behavior, therefore increasing the *CoF*. As a consequence, adherence of proteins from either 3D printed cheese analogue, saliva, or both, as well as the dilution effect largely increased the *CoF*.

3.8. Dynamic sensory evolution

A careful evaluation of consumers' requirements and apprehensions would be essential on account of the launch of foods manufactured by innovative technology. In this sense, understanding consumers' attitudes regarding the sensory profile optimization, personalized nutrition, and consideration of the situational characteristics of serving 3D printed products are considered important parameters toward the acceptance of 3D printed foods. The TDS technique is a procedure established to attain a temporal perception of different traits and offers a comparison of the sensations perceived simultaneously in a complex food product [31]. The evaluation of 3D printed cheese analogues by TDS procedure using a trained sensory panel was suitable to provide a piece of essential information towards the sequence of the dominant sensations in the 3D printed product once processed in the oral cavity. The smoothed TDS plots with the corresponding TDS chance and significance levels are presented in Fig. 7. Each TDS plot displays the evaluated nine attributes of 3D printed cheese analogue variants during the standard time of 100%. In this regard, the chance level (11%) and the significance level (28%) were plotted over the TDS curves according to the binomial distribution and investigating nine sensations and 30 observations. As Fig. 7 demonstrated, among the 3D printed samples, control, PEC1, and PEC2 showed a grainy texture as dominant attributes with a maximum dominance rate (max. DR%) of 42.9%, 47.3%, and 44.4%, respectively, dominating through the entire assessment ($P < 0.05$). This was consistent with the fact these printed samples were characterized by a high level of surface irregularities and the presence of aggregated micro-sized lumps on their surface as revealed by VP-SEM and AFM experiments. In contrast, the graininess in 3D printed PEC3 and PEC4 were not perceived as significantly dominant at any time of evaluation ($P > 0.05$). This might be attributed to the development of a homogenous matrix and uniform structure with a highly porous structure according to the obtained microstructure investigations. Regarding printed PEC3 and PEC4, the firmness and chewiness attributes were more dominant at the middle of the evaluation period as compared to printed PEC1 and PEC2. By referring to the TPA experiment, the instrumental hardness and chewiness of printed PEC3 and PEC4 were notably higher than other samples, which they proposed a denser network structure with strong 3D structural strength.

Concerning 3D printed PEC3 and PEC4, the panelists were also able to perceive the creaminess as a dominant attribute, even with reduced 45% and 60% fat content. This presents useful information concerning the role of micro-biosurfactant in the texture of printed cheese analogue. As a result of the 3D printed structure, the AMCC micro-biosurfactant behaved as a fat substitute and was recognized to show a high oil-binding capacity (as discussed in the DSC and NMR sections). This behavior is on account of existing active acetyl groups, which led to the promotion of a well-defined gel-like structure. On the contrary, the panelist did not detect the creaminess as significantly dominant in the case of 3D printed PEC1 and PEC2 ($P > 0.05$), even though they had higher levels of oil in their formulation compared to printed PEC3 and PEC4. Another promising result regarding the role of AMCC in the texture perception of 3D printed cheese analogue was again assigned to printed PEC3 and PEC4, which showed a thick texture with a max. DR of 50.4% and 55.8%, respectively (Fig. 7). The oral tribology data correlated well with the thickness sensation. The printed PEC3 and PEC4 also experienced the dominance of the smoothness with max. DR of 49.1% and 47.7%, respectively, dominating until the evaluation ended. The hypothesis for explaining this phenomenon might be because the higher levels of micro-biosurfactant induced the lubricating effect during mastication. In the 3D printed samples with the higher AMCC ratios, the mouth-coating was also a significant dominant attribute (with a max. DR of about 56.4%) throughout the evaluation ($P < 0.05$), which offered a desired texture sensation. In the last part of the mastication process, a remarkable residue aftertaste was detected in the printed control, PEC1, and PEC2. This showed the AMCC at the lower contents provided a slightly rougher matrix as compared to the printed PEC3 and PEC4. As previously stated, the AFM roughness parameters (namely R_a and R_q) of printed PEC1 and PEC2 were higher than those of printed PEC3 and PEC4. In this context, printed PEC1 and PEC2 offered a rough surface character, where their topographic micrographs presented uneven and irregular surfaces with the areas containing slits and cracks.

3.9. Correlations between sensory evaluation and instrumental measurements

The requirement for quality control instruments and the desire to predict the consumers' attitudes and to understand what is being perceived in the sensory evaluation are the main fundamentals guiding the research towards sensory–instrumental correlations. In this regard, the PCA was conducted to evaluate the possible correlation between the instrumental readings of 3D printing parameters (namely layer number and line width), surface roughness, thermal behavior, crystallinity degree, mechanical properties, and NMR data with TDS scores extracted from the dynamic sensory properties. This supports to better understanding the role of micro-biosurfactant in the structuring of 3D printed objects [25,44]. TDS score, as a magnitude of sensory attribute intensity, involves both the duration and intensity of dominance. The TDS score for each evaluated attribute was obtained from Eq. (4) during the TDS evaluation. Fig. 8 shows the measured score plot of 3D printed cheese analogues inside each group, in which the PC1 and PC2 defined 51.4% and 14.3% of the variation in the data set, respectively. The 3D printed variants were separated into clusters related to the samples prepared by different ratios of AMCC. The printed PEC3 and PEC4 produced two clusters on the PC1 axis (to right) in the score plot compared to the other samples (Fig. 8a). The PEC1 was also clustered on the left-hand side of the score plot, while printed PEC2 clustered in the middle of the score plot between PEC3 and PEC1. The corresponding loading plot of obtained parameters is also presented in Fig. 8b. The variables located

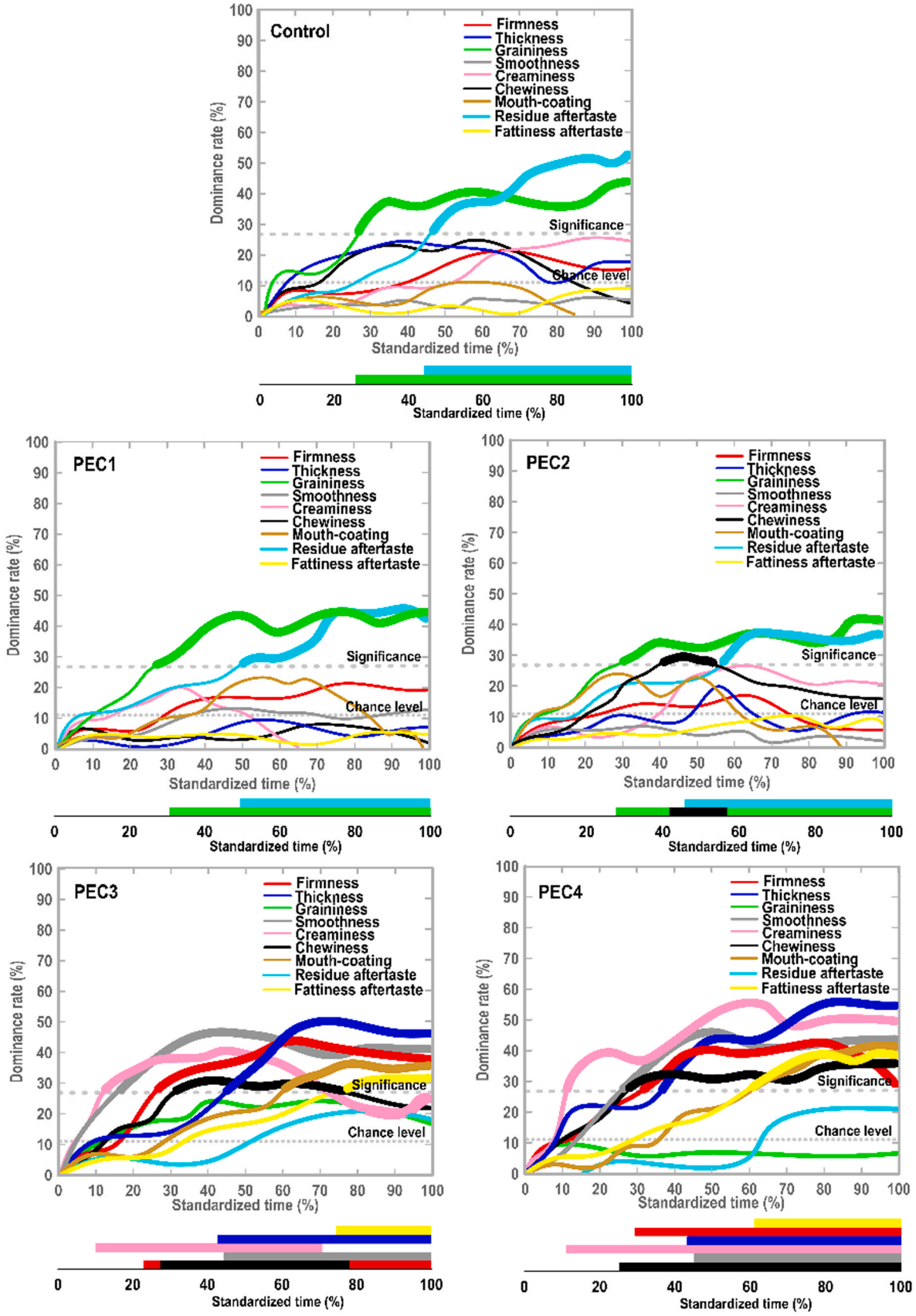

Fig. 7. Temporal profiles of dominant sensations in standardized time with defined sensations in 3D printed cheese analogues variants.

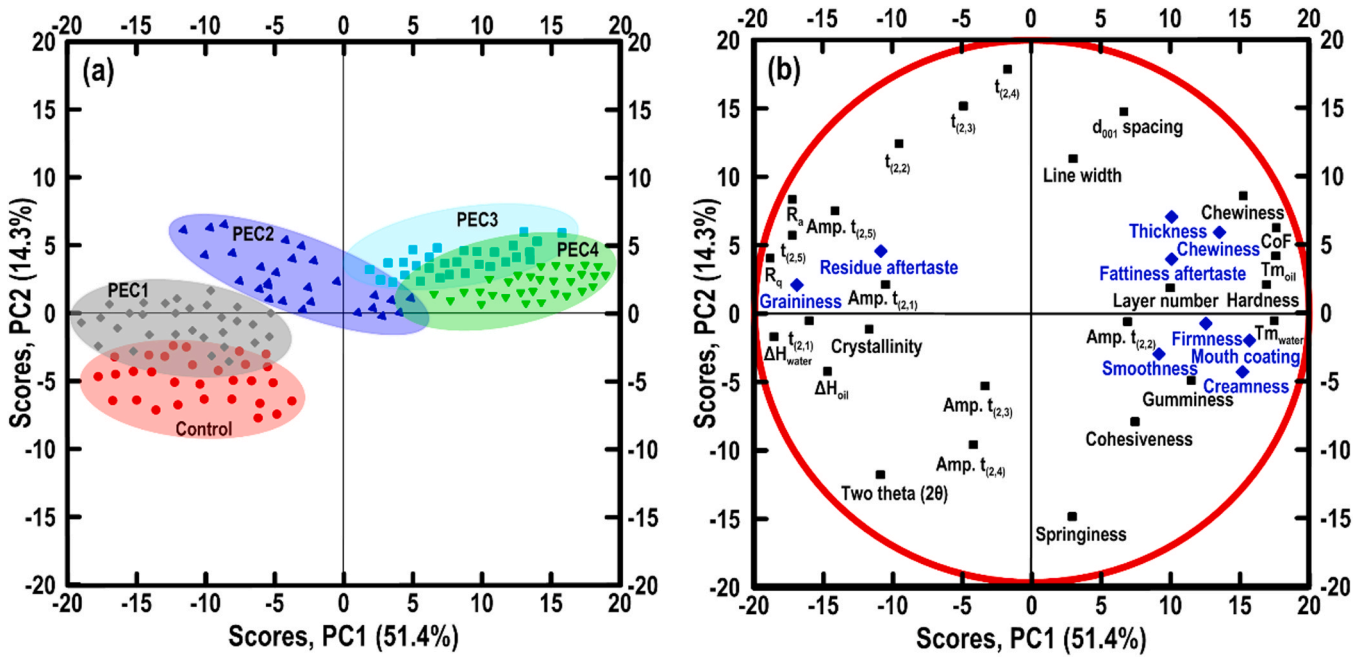

Fig. 8. The PCA correlation of the results from evaluated 3D printed objects representing the first two principal components (PC1 and PC2). (a) Score plot displaying all printed cheese analogues within each group. (b): Correlation loading plot of the measured variables (◆ sensory attributes (TDS score), ■ instrumental measurements).

close to each other display a positive correlation, while the parameters with opposite sign loadings are negatively correlated [25]. The corresponding loading plot was influenced by the instrumental readings of printing performance, thermal, crystalline, tribology, proton mobility, and texture properties, in which the data from the layer number, hardness, gumminess, chewiness, Tm_{oil}, Tm_{water}, *CoF*, and amplitude $t_{(2,2)}$ were represented a positive correlation, which they were located close to each other to the right side of the plot. Furthermore, the PC1 clearly distinguished these parameters as opposed to ΔH_{water}, ΔH_{oil}, crystallinity degree, $t_{(2,1)}$, $t_{(2,5)}$, amplitude $t_{(2,1)}$, amplitude $t_{(2,5)}$, R_q, and R_a (to the left). The corresponding loading plot was also affected by the TDS score of each sensation, in which the sensory assessments of firmness, chewiness, thickness, smoothness, creaminess, mouth-coating, and fattiness aftertaste were limited in the identical part of the correlation loading (to the right), proposing a positive correlation. However, there was a negative correlation between these sensory traits and perceived graininess and residue aftertaste, which were located to the left side of the plot.

The validation of the instrumental measurements and sensory properties is beneficial to understand the exact contribution of instrumental parameters to the complex sensory features, offering the advance of instrumental readings for the specific sensory perceptions [25,44]. The higher predictability of the instrumental readings with sensory variables translates into the most accurate prediction of sensory textural features. In this context, a correlation between the instrumental parameters and the TDS score obtained from the sensory evaluation was conducted (Fig. 8b). The positive correlations were determined among the TDS scores of firmness, chewiness, thickness, smoothness, creaminess, mouth-coating, and fattiness aftertaste and instrumental readings of layer number, hardness, gumminess, chewiness, Tm_{oil}, Tm_{water}, *CoF*, and amplitude $t_{(2,2)}$. This supported the fact that the 3D printed PEC3 and PEC4 cheese analogues would require a greater force necessary to chew the 3D structures. The hardness is an indicator of strength/overall resistance of the 3D printed objects against deformation and gumminess is an index of the energy needed to develop a swallow-able bolus. A positive correlation of these variables with the TDS scores of firmness and chewiness denotes a firm 3D printed sample will need more energy to deform. Conversely, the graininess and residue aftertaste attributes correlated with the crystallinity degree, enthalpy of endothermic peaks, some of the NMR parameters, and surface roughness and negatively correlated with the chewiness, hardness, and gumminess. This indicates that the graininess and residue aftertaste sensations also offered a good estimate of instrumental textural properties, DSC, XRD NMR, and AFM parameters. The swallowing is also related to the textural traits perceived upon the early periods of the oral processing, which varied with different ratios of micro-biosurfactant. It is then concluded the desired firmness, chewiness, and smoothness attributes of the 3D printed cheese analogues with lower graininess and residue aftertaste descriptors required some level of energy to compress and develop a suitable ready-to-swallow bolus. This proposes a desired mixing with saliva and thus might provide the perception of sample creaminess, mouth-coating, and thickness.

4. Conclusion

This work highlighted the potential application of acetylated microcrystalline cellulose in the development of a satisfactory reduced-fat 3D printed cheese analogue. It is concluded the engineering of a high-quality reduced-fat 3D printed cheese requires the application of the applicable micro-surfactant to partially replace the oil portion without unfavorable textural and sensory properties changes. The functional quality of the 3D printed objects strongly related to the ratio of acetylated microcrystalline cellulose since the micro-biosurfactant impacted noticeably on the morphology and printing performance of the printed casein/oil matrix, and consequently on the textural, structural, tribological, thermal, and sensory properties. Increasing the micro-surfactant levels altered the rough and uneven appearance of the original 3D printed object into a smoother and more continuous one. In this sense, the 3D structures in the high resolution were observed with outstanding dimensional stability. The 3D printed objects containing higher levels of micro-biosurfactant showed an enhanced printing performance, mechanical strength, lower crystallinity, and decreased surface roughness with a high level of porosity. The greater stability of the reduced-fat 3D printed objects against freezing was achieved, improving the freeze-

thaw stability of 3D printed architectures. The proton mobility data showed a faster decay and shifting of protons to the shorter relaxation times as affected by the micro-biosurfactant addition, which was coincided with a reduced crystallinity. The oral tribology data revealed the presence of micro-biosurfactant, especially at the higher ratios, achieved a reduction of friction coefficients, indicating a lubrication effect. In view of the in-mouth situations appropriate for the sensory perception, we also explored the effect of saliva on the lubrication, in which the mixing of 3D printed samples with saliva led to an increase in the friction coefficient compared to that one saliva-free product. The results of dynamic sensory evaluation revealed micro-biosurfactant ratio notably varied among the reduced-fat printed cheese analogue and were mainly correlated to instrumental texture parameters. The excellent sensory sensations, especially concerning the temporal perception of creaminess, mouth-coating, and fattiness aftertaste showed the potential of utilization of the reduced-fat 3D printed products conceived as a promising cheese analogue product. This opens for the opportunity of engineering reduced-fat 3D printed products with desired functional features and sensory properties meeting the specific consumer's requirements, as in the case of personalized nutrition, or with the objective to get advanced texture perception.

Funding

Open access funding provided by the University of Natural Resources and Life Sciences Vienna (BOKU).

CRediT authorship contribution statement

Mahdiyar Shahbazi: Conceptualization, Methodology, Investigation, Collecting data, Validation, Data interpretation, Funding acquisition, Writing - original draft, Writing - review & editing. Henry Jäger: Methodology, Writing - review & editing, Supervision. Rammile Ettelaie: Writing - review & editing.

Compliance with ethics requirements

The authors declare no conflict of interest.

Declaration of Competing Interest

The authors declare that they have no known competing financial interests or personal relationships that could have appeared to influence the work reported in this paper.

Appendix A. Supporting information

Supplementary data associated with this article can be found in the online version at doi:10.1016/j.colsurfa.2021.126760.

References

[1] Z. Liu, M. Zhang, B. Bhandari, Y. Wang, 3D printing: printing precision and application in food sector, Trends Food Sci. Technol. 69 (2017) 83–94.
[2] M. Shahbazi, H. Jäger, Current status in the utilization of biobased polymers for 3D printing process: a systematic review of the materials, processes, and challenges, ACS Appl. Bio Mater. (2020).
[3] J. Sun, W. Zhou, D. Huang, J.Y. Fuh, G.S. Hong, An overview of 3D printing technologies for food fabrication, Food Bioprocess Technol. 8 (8) (2015) 1605–1615.
[4] L. Li, Y. Chen, T. Yu, N. Wang, C. Wang, H. Wang, Preparation of polylactic acid/TEMPO-oxidized bacterial cellulose nanocomposites for 3D printing via Pickering emulsion approach, Compos. Commun. 16 (2019) 162–167.
[5] X. Li, X. Xu, L. Song, A. Bi, C. Wu, Y. Ma, B. Zhu, High internal phase emulsion for food-grade 3D printing materials, ACS Appl. Mater. Interfaces 12 (40) (2020) 45493–45503.
[6] C. Kwak, S.Y. Ryu, H. Park, S. Lim, J. Yang, J. Kim, J. Lee, A pickering emulsion stabilized by chlorella microalgae as an eco-friendly extrusion-based 3D printing ink processable under ambient conditions, J. Colloid Interface Sci. 582 (2021) 81–89.
[7] W.J. Long, J.L. Tao, C. Lin, Y.C. Gu, L. Mei, H.B. Duan, F. Xing, Rheology and buildability of sustainable cement-based composites containing micro-crystalline cellulose for 3D-printing, J. Clean. Prod. 239 (2019), 118054.
[8] C. Gauss, K. Pickering, L.P. Muthe, The use of cellulose in bio-derived formulations for 3D/4D printing: a review, Compos. Part C: Open Access (2021), 100113.
[9] E. Dickinson, Biopolymer-based particles as stabilizing agents for emulsions and foams, Food Hydrocoll. 68 (2017) 219–231.
[10] M. Shahbazi, H. Jäger, R. Ettelaie, Application of Pickering emulsions in 3D printing of personalized nutrition. Part I: development of reduced-fat printable casein-based ink, Colloids Surf. A: Physicochem. Eng. Asp. 622 (2021), 126641, https://doi.org/10.1016/j.colsurfa.2021.126641.
[11] N. Lin, J. Huang, P.R. Chang, J. Feng, J. Yu, Surface acetylation of cellulose nanocrystal and its reinforcing function in poly (lactic acid), Carbohydr. Polym. 83 (4) (2011) 1834–1842.
[12] D. Trache, M.H. Hussin, C.T.H. Chuin, S. Sabar, M.N. Fazita, O.F. Taiwo, M. M. Haafiz, Microcrystalline cellulose: isolation, characterization and bio-composites application—a review, Int. J. Biol. Macromol. 93 (2016) 789–804.
[13] E. Dickinson, Emulsion gels: the structuring of soft solids with protein-stabilized oil droplets, Food Hydrocoll. 28 (1) (2012) 224–241.
[14] C. Le Tohic, J.J. O'Sullivan, K.P. Drapala, V. Chartrin, T. Chan, A.P. Morrison, A. L. Kelly, Effect of 3D printing on the structure and textural properties of processed cheese, J. Food Eng. 220 (2018) 56–64.
[15] M.M. Ross, A.L. Kelly, S.V. Crowley, Potential applications of dairy products, ingredients and formulations in 3D printing. Fundamentals of 3D Food Printing and Applications, Academic Press, 2019, pp. 175–206.
[16] K. Daffner, S. Vadodaria, L. Ong, S. Nöbel, S. Gras, I. Norton, T. Mills, Design and characterization of casein-whey protein suspensions via the pH-temperature-route for application in extrusion-based 3D-Printing, Food Hydrocoll. 112 (2021), 105850.
[17] M.A.I. Schutyser, S. Houlder, M. de Wit, C.A.P. Buijsse, A.C. Alting, Fused deposition modelling of sodium caseinate dispersions, J. Food Eng. 220 (2018) 49–55.
[18] Y. Liu, Y. Yu, C. Liu, J.M. Regenstein, X. Liu, P. Zhou, Rheological and mechanical behavior of milk protein composite gel for extrusion-based 3D food printing, Lwt 102 (2019) 338–346.
[19] M. Shahbazi, H. Jäger, S.J. Ahmadi, M. Lacroix, Electron beam crosslinking of alginate/nanoclay ink to improve functional properties of 3D printed hydrogel for removing heavy metal ions, Carbohydr. Polym. 240 (2020), 116211.
[20] M. Majzoobi, M. Shahbazi, A. Farahnaky, E. Rezvani, G. Schleining, Effects of high pressure homogenization on the physicochemical properties of corn starch, in: Proceedings of the InsideFood Symposium, 2013. pp. 33–35.
[21] M. Shahbazi, G. Rajabzadeh, R. Ettelaie, A. Rafe, Kinetic study of κ-carrageenan degradation and its impact on mechanical and structural properties of chitosan/κ-carrageenan film, Carbohydr. Polym. 142 (2016) 167–176.
[22] M. Shahbazi, M. Majzoobi, A. Farahnaky, Impact of shear force on functional properties of native starch and resulting gel and film, J. Food Eng. 223 (2018) 10–21.
[23] M. Shahbazi, G. Rajabzadeh, A. Rafe, R. Ettelaie, S.J. Ahmadi, Physico-mechanical and structural characteristics of blend film of poly (vinyl alcohol) with biodegradable polymers as affected by disorder-to-order conformational transition, Food Hydrocoll. 71 (2017) 259–269.
[24] M. Kiumarsi, M. Shahbazi, S. Yeganehzad, D. Majchrzak, O. Lieleg, B. Winkeljann, Relation between structural, mechanical and sensory properties of gluten-free bread as affected by modified dietary fibers, Food Chem. 277 (2019) 664–673.
[25] M. Kiumarsi, D. Majchrzak, H. Jäger, J. Song, O. Lieleg, M. Shahbazi, Comparative study of instrumental properties and sensory profiling of low-calorie chocolate containing hydrophobically modified inulin. Part II: proton mobility, topological, tribological and dynamic sensory properties, Food Hydrocoll. 110 (2021), 106144.
[26] M. Navazesh, Methods for collecting saliva, Ann. N. Y. Acad. Sci. 694 (1) (1993) 72–77.
[27] P.T. Nguyen, T.A. Nguyen, B. Bhandari, S. Prakash, Comparison of solid substrates to differentiate the lubrication property of dairy fluids by tribological measurement, J. Food Eng. 185 (2016) 1–8.
[28] J.L. Miller, K.L. Watkin, The influence of bolus volume and viscosity on anterior lingual force during the oral stage of swallowing, Dysphagia 11 (2) (1996) 117–124.
[29] K.M. Hiiemae, J.B. Palmer, Tongue movements in feeding and speech, Crit. Rev. Oral. Biol. Med. 14 (6) (2003) 413–429.
[30] ISO (International Organization for Standardization), ISO 8586. Sensory Analysis: General Guidelines for the Selection, Training and Monitoring of Selected Assessors and Expert Sensory Assessors, 2012.
[31] N. Pineau, P. Schlich, S. Cordelle, C. Mathonnière, S. Issanchou, A. Imbert, E. Köster, Temporal dominance of sensations: construction of the TDS curves and comparison with time–intensity, Food Qual. Prefer. 20 (6) (2009) 450–455.
[32] T. Manstan, M.B. McSweeney, Consumers' attitudes towards and acceptance of 3D printed foods in comparison with conventional food products, Int. J. Food Sci. Technol. 55 (1) (2020) 323–331.
[33] M. Shahbazi, M. Majzoobi, A. Farahnaky, Physical modification of starch by high-pressure homogenization for improving functional properties of κ-carrageenan/starch blend film, Food Hydrocoll. 85 (2018) 204–214.
[34] X.F. Zhu, J. Zheng, F. Liu, C.Y. Qiu, W.F. Lin, C.H. Tang, Freeze-thaw stability of Pickering emulsions stabilized by soy protein nanoparticles. Influence of ionic strength before or after emulsification, Food Hydrocoll. 74 (2018) 37–45.
[35] M.T. dos Santos, I.S. Viana, J.N.R. Ract, G.A.C. Le Roux, Thermal properties of palm stearin, canola oil and fully hydrogenated soybean oil blends: coupling experiments and modeling, J. Food Eng. 185 (2016) 17–25.

[36] L. Cornacchia, Y.H. Roos, Stability of β-carotene in protein-stabilized oil-in-water delivery systems, J. Agric. Food Chem. 59 (13) (2011) 7013–7020.
[37] A. Guinier, X-ray Diffraction in Crystals, Imperfect Crystals, and Amorphous Bodies, Courier Corporation, 1994.
[38] C.P. Slichter, Principles of Magnetic Resonance, Springer Science & Business Media, 2013.
[39] P. Mansfield, Symmetrized pulse sequences in high resolution NMR in solids, J. Phys. C: Solid State Phys. 4 (11) (1971) 1444–1452.
[40] J. Chen, J.R. Stokes, Rheology and tribology: two distinctive regimes of food texture sensation, Trends Food Sci. Technol. 25 (1) (2012) 4–12.
[41] J. Chen, Food oral processing—a review, Food Hydrocoll. 23 (1) (2009) 1–25.
[42] H. Czichos, Tribology: A Systems Approach to the Science and Technology of Friction, Lubrication and Wear, Elsevier, 2009.
[43] C.G. Lee, Y.J. Hwang, Y.M. Choi, J.K. Lee, C. Choi, J.M. Oh, A study on the tribological characteristics of graphite nano lubricants, Int. J. Precis. Eng. Manuf. 10 (1) (2009) 85–90.
[44] M. Kiumarsi, D. Majchrzak, S. Yeganehzad, H. Jäger, M. Shahbazi, Comparative study of instrumental properties and sensory profiling of low-calorie chocolate containing hydrophobically modified inulin. Part 1: rheological, thermal, structural and external preference mapping, Food Hydrocoll. 104 (2020), 105698.